Scilight

Thermal Science and Applications
https://www.sciltp.com/journals/tsa

Review

Choice of the Mathematical Models in the Simulation of Elongational Flow-Induced Crystallization (FIC) During Polymer Processing: A Review

Behrang Mohajer, Amirmahdi Salehi, Mohamad Kheradmandkeysomi, Amirjalal Jalali, Markus Bussmann * and Chul B. Park *

Microcellular Plastics Manufacturing Laboratory (MPML), Department of Mechanical and Industrial Engineering, University of Toronto, Toronto, ON M5S 3G8, Canada
* Correspondence: bussmann@mie.utoronto.ca (M.B.); park@mie.utoronto.ca (C.B.P.)

How To Cite: Mohajer, B.; Salehi, A.; Kheradmandkeysomi, M.; et al. Choice of the Mathematical Models in the Simulation of Elongational Flow-Induced Crystallization (FIC) During Polymer Processing: A Review. *Thermal Science and Applications* **2026**, *1*(1), 65–91.

Received: 10 November 2025
Revised: 11 January 2026
Accepted: 12 January 2026
Published: 4 March 2026

Abstract: This review examines mathematical models of elongational Flow-Induced Crystallization (FIC) from a computational modeling perspective, emphasizing their practical integration within transport-based simulation frameworks. The work targets researchers in computational fluid dynamics (CFD) who model the cooling stages of polymer processing operations such as melt spinning and injection molding. Rather than reiterating the extensive physics of FIC, the review focuses on the choice of mathematical formulation best suited for a given simulation objective. Existing approaches are classified into four model types distinguished by their complexity, required input data, and computational cost: Type 1 models introduce empirical crystallization terms within simplified rheological frameworks; Type 2 combine the Avrami formulation with correlations that account for flow-induced effects; Type 3 embed crystallization kinetics directly into constitutive equations through stress or strain tensors; and Type 4 represent molecular or atomistic simulations that resolve chain dynamics in detail. Each model type is critically evaluated in terms of predictive accuracy, implementation practicality, and suitability for different process scales. Comparative tables summarize these attributes, guiding the selection of an appropriate correlation strategy consistent with available data and computational resources. The review concludes by identifying current challenges—including polymer blends, non-isothermal effects, and anisotropic morphologies—and outlining promising directions for future research. Overall, this work serves as a concise reference for CFD practitioners seeking reliable FIC formulations that balance fidelity, efficiency, and applicability across polymer-processing simulations.

Keywords: modeling; crystallization; flow-induced crystallization; flow-enhanced nucleation; simulation

1. Introduction

This review examines mathematical models for elongational flow-induced crystallization (FIC) of polymeric materials and provides guidance for selecting suitable formulations for computational fluid dynamics (CFD) simulations of polymer processing operations such as spinning, blow molding, and injection molding. The discussion focuses on how different model types balance physical fidelity, computational efficiency, and data requirements to match specific simulation scopes.

Crystallization strongly influences the final mechanical, thermal, and optical properties of polymer products. During solidification, the ordered arrangement of molecular chains defines material performance. Among the mechanisms governing this transition, FIC is particularly important because the deformation field accelerates nucleation and directs crystal growth, producing anisotropic morphologies.

FIC has been shown to enable the *in situ* formation of all-polymeric nanocomposites under well-defined shear and elongational flow fields. In particular, shear deformation significantly increases the crystallization temperature of polymer inclusions, enabling the rapid formation and stabilization of nanofibers during processing. In some systems, viscosity enhancement and melt memory effects associated with self-nucleation further amplify FIC, leading to a larger upward shift in crystallization temperature and a narrower crystallization window under shear [1]. In addition, FIC at elevated temperatures promotes molecular orientation, which is essential for achieving effective mechanical reinforcement in flow-processed polymer systems [2].

Under elongational flow, FIC generates the characteristic shish–kebab structures, where fibrillar "shish" backbones align with the flow and lamellar "kebabs" grow radially from them, as illustrated in Figure 1.

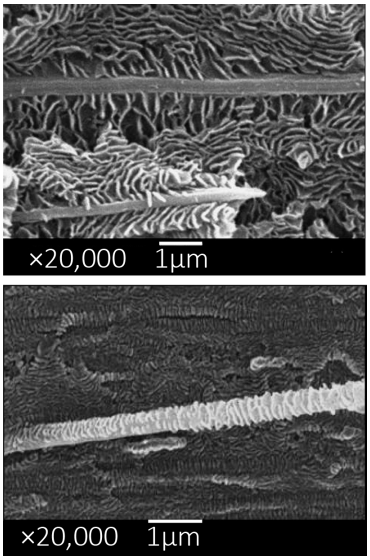

Figure 1. Crystalline structure formation under high-flow conditions: shish–kebab morphology in entangled polymer melts. Reprinted with permission from Ning et al. [3]. Copyright 2007 American Chemical Society.

Figure 2 schematically depicts several common polymer-processing operations involving elongational FIC. In all these processes, the molten polymer exits a die and cools in a downstream region where elongational deformation is a principal factor. Various polymer-processing techniques such as Melt Spinning (MS), Spunbonding (SB), Melt Blowing (MB), Injection Molding (IM), and Blow Molding (BM) are illustrated in Figure 2. In all these operations, elongational deformation in the cooling region governs both stress development and crystallization kinetics.

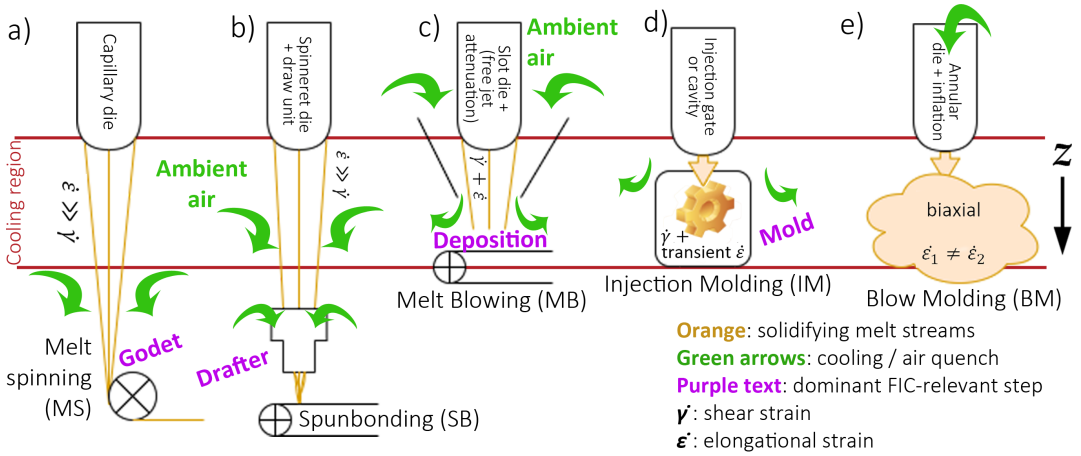

Figure 2. Schematic comparison of polymer processing routes involving flow-induced crystallization (FIC), highlighting differences in die geometry, dominant deformation modes, and cooling conditions: (**a**) melt spinning (uniaxial elongation), (**b**) spunbonding (air-assisted draw), (**c**) melt blowing (high strain-rate elongation), (**d**) injection molding (transient shear and elongation), and (**e**) blow molding (biaxial stretching).

We examined a wide range of earlier reviews and monographs on polymer crystallization and processing, summarized in Table 1. These works cover topics such as Avrami kinetics, non-isothermal crystallization, and flow-induced morphology, but none provide systematic guidance for selecting mathematical models suited

for computational simulations. In particular, the available reviews either emphasize experimental observations, molecular-scale descriptions, or specific processes, while the coupling of crystallization kinetics with transport equations—especially under elongational flow—remains insufficiently discussed.

Table 1. Chronological overview of key review articles, dissertations, and books relevant to polymer crystallization and flow-induced crystallization (FIC), highlighting their primary scope and distinctive contributions.

Ref.	Primary Focus and Distinctive Contribution
[4]	Determination of Avrami parameters in crystallization modeling.
[5]	Comprehensive overview of industrial fiber-processing techniques and the morphology.
[6]	Non-isothermal quiescent crystallization kinetics & experimental validation of Avrami descriptions.
[7]	Modeling approaches for non-isothermal crystallization during polymer processing.
[8]	Unified treatment of thermal and athermal crystallization kinetics in polymers.
[9]	Enthalpic and entropic barriers in crystallization, including Hoffman–Lauritzen theory.
[10]	Simplified lattice-based models for polymer crystallization mechanisms.
[11]	Experimental evidence & interpretation of shish–kebab under high shear and elongational flow.
[12]	Dynamics of fiber formation and coupling between flow kinematics and solidification.
[13]	Overview of classical and molecular-dynamics approaches to polymer crystallization.
[14]	Review of spunbonding technology, process design, and industrial relevance.
[15]	Rheological constitutive models suitable for CFD simulations of polymer processing.
[16]	Review of polymer-chain crystallization models across length and time scales.
[17]	Multiscale modeling of FIC
[18]	Engineering aspects and components of spunbonding processes.
[19]	Classification of polymer crystallization scenarios under thermal and flow conditions.
[20]	Molecular-dynamics simulations elucidating crystallization mechanisms at the chain level.
[21]	Atomistic simulation approaches for polymer nanocomposites and crystallization behavior.
[22]	Activation-energy analysis methods for polymer crystallization kinetics.
[23]	Experimental and modeling studies on elongational flow effects in polymer systems.
[24]	Recent molecular-dynamics insights into segmental alignment, precursors, and shish formation.
	Selected Review Articles Focused on Flow-Induced Crystallization (FIC)
[25]	Early experimental investigations of crystallization mechanisms under flow.
[26]	Comprehensive treatment of FIC, rheology, and two-dimensional space-filling models.
[27]	Experimental observations of flow effects on polymer crystallization kinetics.
[28]	Analysis of Avrami-type behavior observed under flow-induced crystallization conditions.
[20]	Molecular-dynamics perspectives on FIC and flow-driven chain orientation.
[29]	Advanced simulation and multiscale modeling approaches for FIC.
[30]	Molecular-network deformation mechanisms governing FIC in isotactic polypropylene.
[31]	Rheological classification and modeling framework underlying the Peters correlation (Equation (38)).

Despite the breadth of these contributions, no single work provides a structured comparison of existing FIC correlations from the viewpoint of the simulation setup. The present review addresses this gap by organizing available models into four categories based on their analytical formulation and the number of empirical constants involved. Each category is evaluated for its suitability to CFD coupling, allowing readers to choose the most appropriate correlation for a given process, dimensionality, and computational capacity.

The region where crystallization occurs is referred to as the *cooling region*, where the polymer melt exchanges momentum and energy with its surroundings while solidifying. The overall force and energy balances may be symbolically expressed as:

$$\sum F = F_{\text{pressure}} + F_{\text{Godet/Blower}} + F_{\text{viscous}} + F_{\text{drag/friction}} + F_{\text{weight}} + F_{\text{surface}}, \tag{1}$$

$$\Delta E_{\text{total}} = W_{\text{Godet/blower/flow}} + W_{\text{viscous}} + W_{\text{drag}} + W_{\text{gravity}} + W_{\text{surface}} + Q_{\text{convection}} + Q_{\text{fusion}} + Q_{\text{radiation}}. \tag{2}$$

These terms highlight the multiple interactions among flow, heat, and phase transformation that a model must capture. In polymer processing simulations, flow-induced crystallization is strongly governed by the local thermal history, as heat transfer, latent heat release, and temperature-dependent rheology jointly control crystallization

kinetics and stress development.

For practical simulations, such equations are typically simplified; therefore, the degree of simplification serves as one metric for classifying the models reviewed here.

The rheological constitutive model governs the stress–velocity coupling and must be consistent with the level of overall model complexity. We listed multiple models commonly adopted among fluid dynamic researchers in Table 2.While isothermal rheology is well established and supported by several open-source tools (e.g., [32,33]), cooling-induced crystallization introduces additional elastic effects that significantly influence flow behavior. As the melt cools, the relaxation time λ increases, enhancing stress transfer and reinforcing crystallization [12,34]. Figure 3 plots strain and viscosity parameters, marking the characteristic relaxation times that will be further discussed in Section 3. These regimes highlight how molecular stretching and entanglement affect the elongational viscosity, which in turn complicates the numerical stability and computational cost of detailed rheological–crystallization coupling.

Table 2. Representative rheology models used in FIC simulations.

Rheology Model	Dim.	Mathematical Tool	Governing Equation
Newtonian	$1D$	Curve-fit η_q–T	$\sigma = \eta(T) \cdot f(\text{strain})$
Generalized Newtonian	$1-3D$	Combined $\dot{\varepsilon}$ & $\dot{\gamma}$	$\underline{\sigma} = f(T, \eta, \underline{D})$
Maxwell	$3D$	Spring–dashpot	Elastic and viscous
Upper Convected Maxwell (UM)	$2D$	Reduced matrix dimension	$N_{11} = \sigma_{xx} - \sigma_{rr}$
Giesekus	$1-3D$	Extended momentum	λ, viscous and polymer η
Doi–Edwards	$1-3D$	Multi-spring model	Multi-bead
Suspension (rheometry) [1]	$1D$	Melt-phase interaction	$\frac{\eta}{\eta_{\text{amorph}}} = \left[1 - \frac{\chi}{\text{const}}\right]^{\text{const}}$
Pom–pom and extended	$2-3D$	Conformation	$\Lambda = \sqrt{\mathbf{tr}\underline{C}}$
Refer to [15,26,35] for comprehensive listings.			

[1] Filling factor $\chi(t)$ can be obtained from rheometry via $\chi(t) = \frac{G'(t)-G'(0)}{G'(\infty)-G'(0)}$ [36].

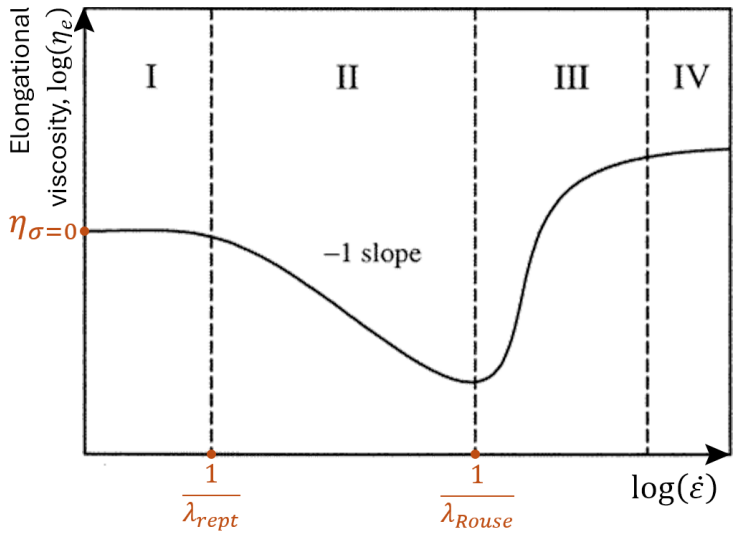

Figure 3. Variation of elongational viscosity with strain rate, showing four characteristic regimes due to chain stretching and entanglement. Reprinted with permission from Marrucci and Ianniruberto [37]. Copyright 2004 American Chemical Society.

Simplified approaches such as suspension theory [38] treat the crystalline phase as dispersed within an amorphous matrix, linking viscosity to crystallinity χ. Although numerically efficient, such formulations may compromise stability in complex geometries. Generalized Newtonian models often assume similar behavior in shear and elongation, an acceptable approximation in thin geometries where thermal gradients dominate strain effects [39].

A recurring trade-off between model accuracy and computational cost has been widely reported in CFD-based simulations of polymer processing and flow-induced crystallization [15,26]. The optimal balance depends on the process, available data, and simulation objectives. This review identifies these trade-offs across the literature to aid in model selection [40].

We introduce the fundamental concepts of crystallization in Section 2, where models are classified by their analytical formulation and empirical input parameters (denoted as *const*). Increasing the number of such parameters generally enhances predictive accuracy but reduces the model's adaptability across materials and processes. Therefore, the present study emphasizes how this balance between accuracy and generality guides the selection of an appropriate FIC correlation. Rather than classifying models solely by physical mechanisms, we categorize available formulations according to their mathematical structure, level of empirical input, and compatibility with transport equations for momentum, energy, and rheology. This classification framework is intended to guide model selection for process-scale simulations, enabling readers to identify formulations that balance physical fidelity, computational cost, and data availability. Each subsequent section concludes with comparative tables summarizing the reviewed models.

2. Physics of Crystallization

In quiescent, isothermal cooling at constant ambient temperature (T_a), a polymer melt crystallizes below the melting temperature T_m. As chains reorganize into ordered structures, crystallization initiates near T_c and proceeds down to the glass transition T_g, yielding a semicrystalline solid. We denote the crystalline mass fraction by χ, which increases from 0 toward the maximum absolute crystallinity χ_∞; the remaining fraction $1-\chi$ is amorphous.

The Avrami equation [41] has been widely used as a kinetic model for polymer crystallization [5], often showing good agreement across materials [42]. In its simplest application, nucleation is idealized and growth is treated as isotropic (spherulitic). We use "Avrami" broadly to include later forms (e.g., Nakamura) that retain the same conceptual structure. The basic relation is

$$\frac{\dot{Q}(t)}{\dot{Q}_{total}} = \frac{\chi(t)}{\chi_\infty} = \theta(t) = 1-\exp[-k(T)\,t^n], \qquad n,\ k \quad \text{are two} \quad const\text{s}. \tag{3}$$

Here $\dot{Q}$ is the heat flow, θ the relative crystallinity, n an exponent related to nucleation and growth geometry, t the elapsed time, and $k(T)$ an empirical function of T encompassing nucleation and growth kinetics. Using θ instead of χ leverages calorimetric data (e.g., DSC), and reference values for $\chi = 1$ exist for many polymers (e.g., [43]). The induction time t_{ind} precedes measurable growth, and the crystallization half time $t_{1/2}$ is commonly extracted from DSC. Figure 4 illustrates typical isothermal behavior and its T–t mapping context for simulations.

In practice, simulations are non-isothermal, so isothermal measurements are often used to calibrate a T–t mapping that recovers $\theta(t)$ along a computed $T(t)$ trajectory. A common approach fits experimental *const*s in an induction-time relation and then applies it during cooling:

$$t = t_{\text{total}} - t_{\text{ind}}^{\text{iso}}, \qquad t_{\text{ind}}^{\text{iso}} = const\cdot(T_m - T)^{const}\ \ [44], \tag{4}$$

with extensions to non-isothermal cases such as

$$t_{\text{ind}} = \int \frac{dT}{\beta}\ \ [45], \qquad t_{\text{ind}} \propto \dot{N}\ \ [46], \qquad t_{\text{ind}} \propto \tfrac{1}{\dot{\varepsilon}}\ \ [47]$$

Here β is the cooling rate; $\dot{N}$ and $\dot{\varepsilon}$ indicate nucleation rate and elongation rate, respectively.

The scope and limitations of Avrami are well known [48, 49]: (i) it is grounded in isothermal kinetics; (ii) estimating χ_∞ is required; (iii) idealized nucleation/growth assumptions must be adapted for impingement and regime competition; and (iv) it does not by itself encode melt squeezing, chain folding, or cross-linking. Numerous extensions address these points (e.g., [6, 50–52]). Table 3 lists selected quiescent milestones spanning k, growth rate G, nucleation $\dot{N}$, thermodynamics (K, β, $\mathbb{G}$, …), and geometry.

Process data often need to enter the crystallization description through explicit kinetic or thermodynamic sub-models when aiming at processing relevance. Rather than a universal equation, *categories* of models provide practical references that match project scope and available data.

Many widely used forms (e.g., Equation (13)) combine two exponentials to capture the bell-shaped temperature dependence seen in Figure 4b: one term acts as a diffusional barrier at low T and the other as a thermodynamic drive with supercooling. Because activation energies can evolve during crystallization, isoconversional methods estimate $E_D(T)$ at fixed θ [53]; this improves data description (e.g., [54]) but offers limited mechanistic transferability.

Table 3. Selected milestones in the evolution of Avrami-type developments.

Physical Aspect	Correlation(s)	Explanation of Variables
Spherulitic growth	$k_q = \frac{4\pi}{3} N_q G^3 \quad n_q = 3 \quad (5)$	G is a linear growth rate [5].
From N_q and G to k and $t_{1/2}$	$k_q = \frac{\ln(2)}{t_{1/2}^3}, \quad N_q = \frac{3}{4\pi}\ln(2)\left(\frac{1}{G(t_{1/2})}\right)^3 \quad (6)$	DSC yields k_q and $t_{1/2}$; N_q follows by fitting $G(t)$.
Induction time varies with the type and speed of cooling, and several correlations have been suggested:	Isothermal induction time: $t = t_{\text{total}} - t_{\text{ind}}^{\text{iso}}$, $t_{\text{ind}}^{\text{iso}} = const \cdot (T_m - T)^{const}$ [44] (7) The non-isothermal examples in Equation 4	Experimental calibration provides $const$s for use in simulations.
A dimensionless time $\frac{t}{t_{1/2}}$ was reported to be used to form Avrami master curves [55].		
Competing regimes (phase co-precipitation) Weights w_i represent competing regimes; the many $const$s complicate validation.	$\theta(t) = w_1\left(1 - e^{-k_1 t^{n_1}}\right) + w_2\left(1 - e^{-k_2 t^{n_2}}\right), \quad 1 = w_1 + w_2, \quad (8)$	
Nakamura non-isothermal form [56]	$\theta(t) = 1 - \exp\left[-\left(\int_0^t K(T)ds\right)^n\right]$, $K(T) = (\ln 2)^{1/n}\frac{1}{t_{1/2}} = k(T)^{1/n}$, $\frac{D\theta}{Dt} = nK(T)(1-\theta)\left[-\ln(1-\theta)^{\frac{n-1}{n}}\right]$ (9)	$\frac{D}{Dt}$ is the material derivative; K can vary with t.
Sporadic nucleation and flow activation ($N = N_q + N_f$)	$\theta = 1 - \exp\left[-k_f(T)t^{n_f} - k_q(T)t^{n_q}\right]$, $k_f = \frac{\pi}{3}\dot{N}G^3, \quad (\dot{N} = \dot{N}_f)$ (10)	Under strong flow, $k_q = 0$ and $k_f \neq 0$ have been reported; reported n may shift with mechanism [5].
Rod- and disk-like crystal growth models (illustrative)	$k_q = NGA, \quad n_q = 1$ (Rod); $k_q = 2\pi r\, NG^2, \quad n_q = 2$ (Disk) (11)	r disk radius, A area normal to growth; irregular growth gives continuous n [42].
Ozawa's non-isothermal form [57]	$\theta = 1 - \exp\left[\frac{f(T)}{\beta^n}\right]$, $\beta =$ fixed cooling rate $< 100\frac{K}{\text{min}}$ (12)	f is a simple empirical cooling function substituting $k(T)$ with a few $const$s—this method is limited to a fixed and low cooling rate.
Turnbull and Fisher model (TF) [58] in 1949 addresses details by introducing the nucleation rate.	$\dot{N} = const \cdot \exp\left[\frac{-E_D}{RT}\right] \cdot \exp\left[\frac{-\Delta\mathbb{G}}{RT}\right]$, $\Delta\mathbb{G} = \frac{const}{(\Delta T)^2}$ (13)	E_D, R, and $\mathbb{G}$ are the activation energy of molecular diffusion, the ideal gas constant, and the free energy of nucleation, respectively. $\Delta T = T_m - T$ is the supercooling (undercooling) temperature.

Schneider et al. [59] suggested operator splitting to solve stepwise differential equations, assuming that crystals are spheres that fill up the space. This approach can be applied to shish-kebab and other structure formation under flow with adjustments, while more information about G is known [60].

Differential Equation	Initial Condition	Physics
$\dot{\phi}_3 = 8\pi\dot{N}_q$	$\phi_3 = 8\pi N_q$	Quiescent $\dot{N}$
$\dot{\phi}_2 = G\phi_3$	$\phi_2 = 8\pi R_{\text{crystal}}$	Radius
$\dot{\phi}_1 = G\phi_2$	$\phi_1 =$ total surface	Crystals' surface
$\dot{\phi}_0 = G\phi_1$	$\phi_0 =$ total crystal volume	Crystals' volume
$\phi_0 = -\ln(1-\chi_q)$	Impinging spherulitic	Space filling
$\chi_q = 1 - \exp\left[-\frac{4\pi}{3}G^3 N_q t^3\right]$	Spaces filled with grown crystals	Quiescent solution with no morphology
General solution [61]:	$\chi_q(t) = 1 - \exp\left[-const_{\text{shape}}\int_0^t \left(\dot{N}_q(v) + \dot{N}_f(v)\right)\cdot\left(\int_0^t G(u)\cdot du\right)^n \cdot dv\right]$ (14)	

Hoffman–Lauritzen (HL) [62,63]

$$K(T) = [\ln(\tfrac{1}{2})]^{1/n}\frac{1}{t_{1/2}} = const_t \exp\left[\frac{-U^*}{R(T-T_\infty)}\right]\exp\left[\frac{-K_t}{Tf\Delta T}\right],$$
$$G = const_G \exp\left[\frac{-U^*}{R(T-T_\infty)}\right]\exp\left[\frac{-K_G}{Tf\Delta T}\right], \quad K_t = const\cdot\frac{T_m}{\Delta H}, \quad f = \frac{2T}{T+T_m} \quad (15)$$

Here U^* is a universal constant, ΔH the heat of fusion, f a melt-property correction, and T_∞ a temperature well below T_g where crystallization ceases. Measuring K and G, Lamberti [64] evaluated overall coefficients (K_t, K_G) operationally associated with kinetic and thermodynamic contributions.

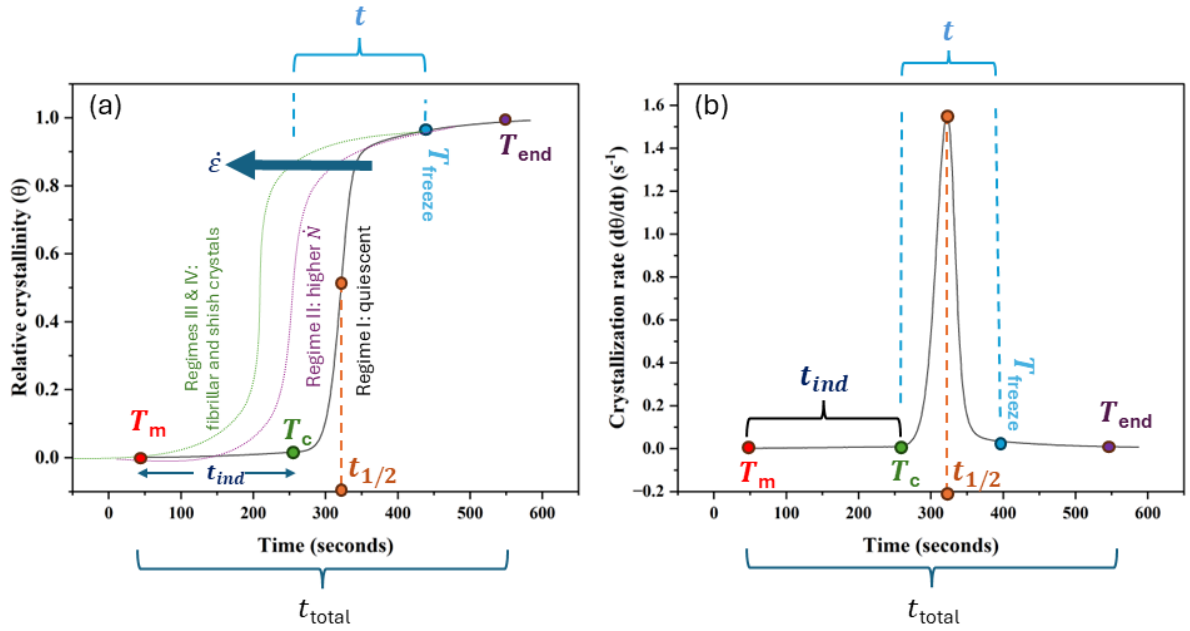

Figure 4. Isothermal crystallization rates for different crystallization regimes of iPP over time (measured at MPML). Critical temperatures annotate the T–t relationship. (**a**) $\theta(t)$; (**b**) quiescent isothermal rate from DSC. In processing simulations, non-isothermal conditions prevail, and local material derivatives $\frac{D\theta(x,y,z,t)}{Dt}$ are required.

Among growth-rate formulations, HL (Equation (15)) remains prevalent; see [9] for regime competition and related barriers. Complex non-isothermal fits with many $const$s (e.g., [65,66]) can capture multiple regimes but are costly to generalize. A practical formulation used by Mubarak et al. [7] combines dual-regime Avrami (Equation (8)) with an induction-time map (Equation (4)), and Hammami's set [67] (Equation (16)):

$$\begin{aligned}
&\theta(t) = 1 - \exp[-K(T)\, t^n]\,, \\
&\theta(T) = 1 - \exp\left[-K(T)\left(\frac{T_c - T}{\beta}\right)^n\right], \\
&K(T) = \text{Equation (15)}, \qquad \beta(t) \in \left[1, 100\frac{K}{\min}\right], \qquad n = 3, \\
&\sum_0^{t_{\text{ind}}} \frac{\Delta t}{t_{\text{ind}}^{\text{iso}}} = \sum_{T_m}^{T_c} \frac{\Delta T}{\beta \cdot t_{\text{ind}}^{\text{iso}}} = 1 \quad \text{(Equation (4))}.
\end{aligned} \tag{16}$$

In this formulation, $K(T)$ embeds $G(T)$, nucleation is implicit, and the non-isothermal t_{ind} is obtained from the isothermal $t_{\text{ind}}^{\text{iso}}$ via the cumulative relation. This provides a workable bridge from DSC-calibrated kinetics to simulation time lines.

Next in Section 3, we extend to FIC models and their rheological assumptions, preparing for the model-selection framework (Types 1–4) used later in this review.

3. Flow-Induced Crystallization (FIC)

Flow markedly alters crystallization [60,68], affecting kinetic parameters (k, n, t), the attainable crystallinity (χ_∞), thresholds $(T_c,\ \sigma_{\text{yield}})$, and microstructure $(G,\ N)$. These effects have been probed by in-situ optical imaging [69, 70], WAXS [71], image analysis [72, 73], stress measurements [74, 75], and rheometry [76, 77]. Understanding FIC is therefore essential for predictive simulations of polymer solidification.

Flow increases chain orientation and contact probability for stem formation, activating additional nucleation sites and biasing growth direction along the principal stretch (Figure 5). The resulting anisotropy enables property enhancement but also modifies the melt response compared with quiescent crystallization. Chain reorientation lowers configurational entropy and produces elongational strain-hardening. Part of the mechanical input is stored elastically in the entanglement network and conformation, contributing to the internal energy; its relaxation during flow can shift effective barriers (e.g., observed changes in T_c) under FIC conditions.

A mesoscale picture is provided by the Doi–Edwards (DE) framework [78,79], which represents chains as multi-bead springs (rod-like segments connected by springs). Extensions separate nucleation $\dot{N}$ from growth G and add them explicitly to modified Nakamura-type kinetics in the form of Equation (9) (e.g., [80,81]), acknowledging

that drawing rate influences $\dot{N}$ (activation/orientation) and G (directional, often cylindrical growth) differently. Interdependence between $\dot{N}$ and G motivates molecular-to-macro coupling; see [5,16] for molecular-level rate discussions, with qualitative outcomes summarized in Table 4.

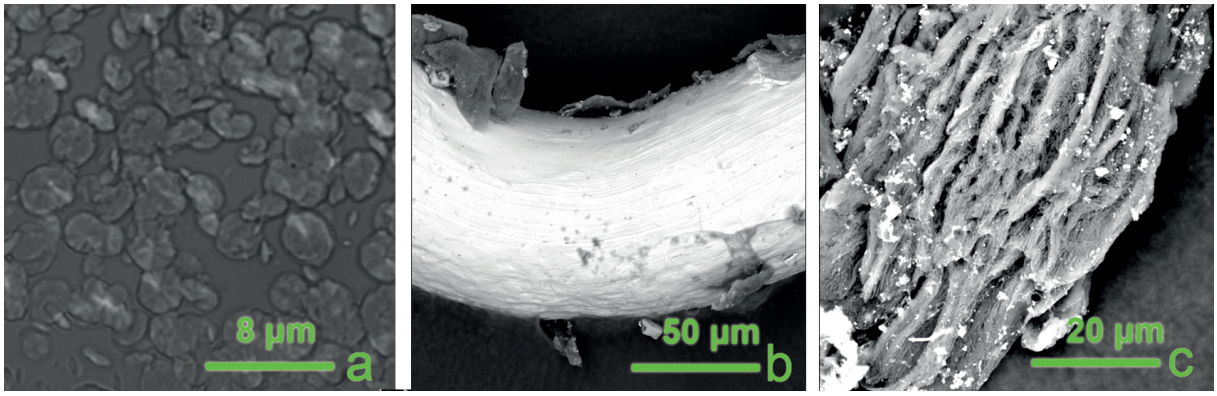

Figure 5. Electron microscopy images of PP crystallization captured by the authors at MPML: (**a**) quiescent crystallization, showing spherulitic structures embedded in the amorphous phase; (**b**) spunbonded PP fiber exhibiting flow-induced crystallization; (**c**) higher-resolution image of a spunbonded fiber after partial etching, highlighting pronounced directional crystallization induced by elongational deformation. All images correspond to laboratory-scale processing conditions representative of industrial spunbonding.

Although shear-induced and elongation-induced crystallization share features, the literature coverage is uneven, with far fewer studies focused on elongational FIC [82].

Two characteristic thresholds are commonly discussed (Figure 6a): a reptation-related threshold and a Rouse-stretch threshold (e.g., [83–86]). At low strain rate or short deformation time, only entangled sections relax via reptation; at higher rates/times, chains disentangle and undergo finite extensibility. Dimensionless groups used to organize these effects are

$$\begin{aligned} De &= \frac{\text{characteristic time}}{\text{observing time}} = \frac{\lambda}{t}, \\ Wi &= \dot{\varepsilon}\,\lambda, \\ De_{\text{rept}} &\equiv Wi_{\text{rept}} = \dot{\varepsilon}\,\lambda_{\text{rept}}, \\ De_{\text{Rouse}} &\equiv Wi_{\text{Rouse}} = \dot{\varepsilon}\,\lambda_{\text{Rouse}}, \\ \lambda_{\text{Rouse}} &\propto Z^2, \qquad \lambda_{\text{rept}} \propto Z^3, \end{aligned} \tag{17}$$

where Z denotes the number of entanglements per chain (Figure 6b). Reported estimates for their ratio include $\lambda_{\text{rept}} \approx 3Z\,\lambda_{\text{Rouse}}$ [87] as well as the similar correaltion of $\frac{\lambda_{\text{rept}}}{\lambda_{\text{Rouse}}} = 3Z\left(1 - \frac{1.51}{\sqrt{Z}}\right)^2$ [78]. The regime boundaries also appear in elongational rheometry (Figure 3). At very high $\dot{\varepsilon}$, elongational thinning can occur when chains approach full stretch and slide past one another [88,89].

Wi and De encode different perspectives: Wi reflects the local deformation rate, whereas De compares relaxation with the process timescale. Along a Lagrangian trajectory at fixed Wi, De typically decreases downstream as the local observing time grows. Mechanical work has also been used as a single measure that correlates with orientation and crystallization [90,91], with elongational flows requiring less work than shear to achieve similar crystallization [92].

In this study we categorize FIC literature according to how deeply these formulations are used (Table 4), from Type 1 (empirical add-ons) to multi-dimensional Type 2 (Avrami plus one flow-sensitive correlation), to Type 3 (stress-tensor based coupling of rheology and kinetics), and Type 4 (molecular/atomistic contour simulations). The categories reflect increasing analytical detail and typically require different numbers of $const$s.

Next, we review each type in turn, emphasizing model-selection trade-offs (accuracy versus adaptability), and highlighting novel correlations for G, $\dot{N}$, T_c, and η relevant to elongational FIC.

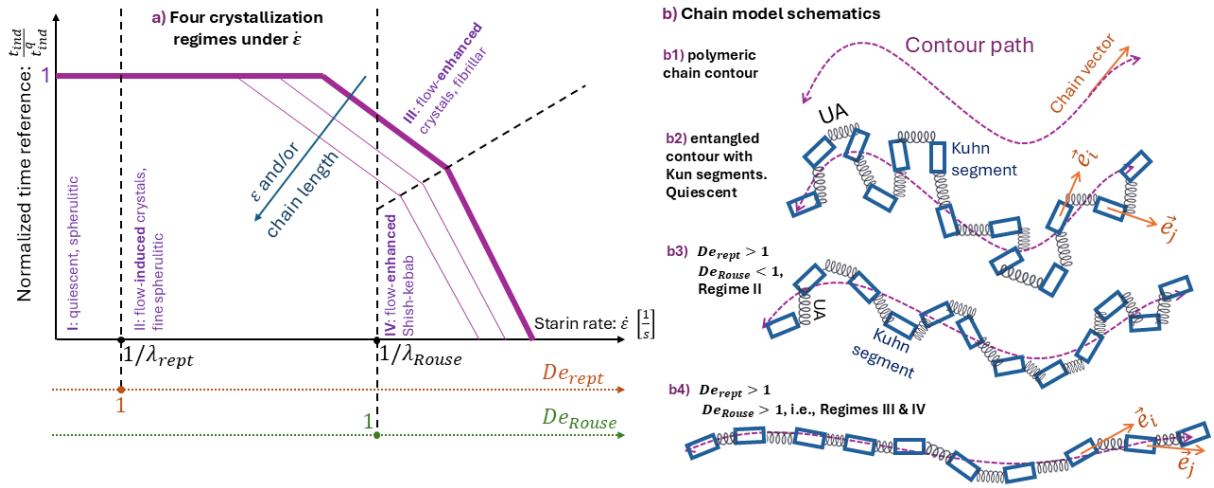

Figure 6. Crystallization and chain behavior versus strain rate. (**a**) Four qualitative regimes classified by De, with transitions near the reptation and Rouse relaxation times [31]; sketch based on [87]. (**b**) Chain representation: (**b1**) contour; (**b2**) rigid Kuhn segments with unit vectors $\vec{e}_i$; (**b3**) for $De_{\text{rept}} > 1$, reorientation ("snake-like") induces flow-activated nucleation; (**b4**) for $De > \lambda_{\text{Rouse}}$, chains stretch axially, favoring cylindrical growth and flow-enhanced crystallization; extreme stretch can induce segment rotation/isomerisation [87].

Table 4. $\dot{N}$ and G during crystallization, qualitative regimes versus strain rate, and summary of FIC model types used in this review.

Quiescent	**Onset**	**Middle**	**End/Freezing**	
t	Low (start of bell shape)	$\approx t_{1/2}$	High	
T	High (just below T_m)	$\approx T_{1/2}$	Low (near/above T_g)	
$\dot{N}$ and G	$\dot{N} \ll G$	$\dot{N} \approx G$ [1]	$\dot{N} \gg G$	
$\dot{\varepsilon}$ **regime** [2]	**Avrami parameters in Equation (14)**	**Physics**	$De = \lambda/t$ [3]	**Structure**
I	$\dot{N}_q, G_q, n = 3, k_f$	Section 2	$De_{\text{rept}}, De_{\text{Rouse}} < 1$	Coarse spherulitic
II	$\dot{N}_q + \dot{N}_f, G_q, n = 3, k_q$	Orientation	$De_{\text{Rouse}} < 1 < De_{\text{rept}}$	Fine spherulitic
III	$\dot{N}_q + \dot{N}_f, G_q \to G_f, n \in (2,3), k_q \to k_f$	Stretch	$1 < De_{\text{rept}}, De_{\text{Rouse}}$	Fibrillar/sausage [93]
IV	$\dot{N}_q + \dot{N}_f, G_f, n \approx 2, k_f$	Isomerisation	$1 < De_{\text{rept}}, De_{\text{Rouse}}$	Shish–kebab
FIC Type	**Correlation(s)** [4]	**Accuracy**	**Adaptability**	**No. *consts***
Type 1	Ignoring $\dot{N}$, G, and T_c	Low	High	Few
Type 2	Avrami Equation (9) + one of $\dot{N}$, G, or T_c	Medium	Medium	High
Type 3	Mixed elongation & shear via $\underline{\sigma}$	High	Low	Medium
Type 4	Molecular and mesoscale dynamics (MD)	High	Very low	Medium

[1] Qualitative comparison regardless of units. [2] See, e.g., [31,68,94]. [3] Many studies also use $Wi = \dot{\varepsilon}\lambda$ to represent molecular stretch; De emphasizes the time-scale ratio and strain-duration effects [87]. [4] Types are introduced and compared in this review.

3.1. Type 1: Empirical Model

Type 1 models comprise $1D$ empirical approaches that prioritize simplicity and transferability over detailed crystallization physics. They adapt readily to different throughputs, require minimal experimental input, and can be ported across processes. A representative starting point is Hsiung et al. [44], who determined a $const$ (e.g., $k_{1/2}$) using quiescent Avrami fits; a commonly used set is

$$\begin{aligned}
\theta(t) &= 1 - \exp\left[-\ln(2)\left(\frac{t}{t_{1/2}}\right)^{n}\right] && [76] \\
k(T) &= k_{1/2} \cdot \exp\left[-4\ln(2)\left(\frac{T - T_{1/2}}{T_c - T_{\text{freezing}}}\right)^{2}\right] && [95] \\
k(T,\sigma) &= k(T) \cdot \exp\left[const \cdot \sigma^{2}\right] && [96] \\
k(T,\sigma) &= k(T) \cdot \exp\left[\sum_i const_i \cdot \sigma^{2}\right] && \text{multi-mode/polydisperse}
\end{aligned} \tag{18}$$

where σ is the stress; flow-related kinetics (k_f, k_q) are lumped into an empirical k. The peak rate $k_{1/2}$ corresponds to the DSC maximum near $T_{1/2}$ (midway between T_c and T_{freezing}). Fits may use DSC, microscopy, WAXS, and/or rheometry to determine $const$s. Heterogeneous crystallization (nucleants, binders, additives, recycled content) also

alters kinetics [97–99]; in Type 1, it is practical to combine k_f and k_q into a single k to reduce parameters during fast cooling.

Stolin et al. [100,101] advocate a phenomenological kinetic equation written directly for the rate of crystallization as a function of conversion. This equation yields an integral solution close to the Avrami law while being more suitable for non-isothermal and engineering calculations:

$$\frac{d\theta}{dt} = k\theta^n(1-\theta) \Rightarrow \theta(t_{\text{crystal}}) = \int_0^{t_{\text{crystal}}} k(T)\cdot\theta^n\cdot(1-\theta)\cdot dt \tag{19}$$

where n and k are fitting $const$s regardless of the shape of the nuclei, and unlike Avrami, $\frac{d\chi}{dt}$ is not a function of t anymore.

Because Equation (18) is compact, it can be advanced alongside complex rheology with few numerical difficulties in applied CFD (e.g., [38]). A frequent implementation updates the Avrami rate coefficient K in Equation (9) via an empirical stress-based factor; effects on $\dot{N}$ or T_c are neglected:

$$\begin{aligned} K &= K_q\cdot\exp\left[const\cdot N_{11}^{const}\right] \qquad K \xrightarrow{\text{Equation (15)}} G \\ K &= K_q\cdot\exp\left[\sum_i const_i\cdot N_{11}^{const_i}\right], \quad i=1,2,\dots \\ N_{11} &= \sigma_{xx}-\sigma_{yy} \;\approx\; \eta\,\frac{\partial V}{\partial x} \quad \text{in } 1D \text{ steady state.} \end{aligned} \tag{20}$$

Here N_{11} is the first normal-stress difference along the elongation direction and V the axial velocity. The multimode form captures multiple elongational regimes [31,102] given a known velocity field.

Another common Type 1 variant augments a generalized-Newtonian viscosity with a crystallinity-dependent factor (a "Ziabicki-type" coupling), long used in spinning [12,103]:

$$\begin{aligned} \eta_e(T,\chi) &= \eta_e(T)\cdot\exp\left(const\cdot\chi^{const}\right) \\ \eta_e(T,\chi) &= \eta_e(T)\cdot\left(1+const\cdot\chi\right) \\ \eta_e(T,\chi) &= \eta_e(T)\cdot(1-\theta)^{-const} \qquad [104] \end{aligned} \tag{21}$$

These forms are appropriate when deformation effects on viscosity are small; Pantani et al. [105] noted that χ can act as a shift factor for both deformation and zero-shear viscosity. In thin, convection-dominated fiber flows, using $\chi(T)$ and a heat-transfer model often suffices. Zhao [106] and Kanai et al. [107] demonstrate applied elongational cases. Inspired by [107], we adopted

$$\eta_e(T,\theta) \;=\; 3\,\eta(T)\cdot f(const\cdot\theta) \quad \text{with Newtonian } \eta_e = 3\eta, \tag{22}$$

where f is a numerical adjustment; $\eta(T)$ may also include strain-rate dependence (e.g., Carreau–Yasuda) if desired, though Type 1 generally avoids additional $const$s.

A theoretical alternative is the step-wise isoconversional approach [108], which prescribes an $E_D(T)$ distribution. While powerful for quiescent crystallization [49,61], we found no applied FIC simulations using it. We also note Chen et al. [109], who trained a machine-learning model on experiments to predict PP fiber diameter—an empirical pathway consistent with Type 1.

Classic spinning formulations by Kase–Matsuo [110] and Beyreuther–Brünig [12] further illustrate Type 1 with simplified momentum/energy balances and various $\eta(T)$ choices, yielding quick estimates of axial velocity $U(x)$ under FIC couplings.

Nie et al. [111] showed that flow modifies conformation entropy (relaxation), orientation entropy (available nucleation surface), phase-transition enthalpy (contact area), and solid-state enthalpy (e.g., shish), thereby shifting crystallization free energy [17,112]:

$$\Delta\mathbb{G}_f \;=\; const_{\text{Fold}}\cdot const_{\text{Surface}}\cdot const_{\Delta H}\cdot\Delta\mathbb{G}_q \tag{23}$$

with each $const$ linked to the corresponding entropy/enthalpy change. Follow-up MD studies [24] provide chain-level support (see Section 3.4).

Overall, Type 1 is usually one-dimensional, fast, and practical for applied and industrial studies. It favors experimental calibration and can approximate secondary dimensions (e.g., 1.5D die-swell in [38]). It is well-suited

to new throughputs/blends when computational effort is reserved for rheology, and it can be implemented with modest CFD expertise. Table 5 summarizes the main options.

Table 5. Pros and cons of Type 1 models.

Type 1 Model	Equation	Comments
$\theta(t) = 1 - \exp\left[-\ln(2)\left(\frac{t}{t_{1/2}}\right)^n\right]$	(18)	Minimal inputs; suitable when FIC is weak or treated implicitly.
$k(T) = k_{1/2}\exp\left[-4\ln(2)\left(\frac{T-T_{1/2}}{T_c-T_{\text{freezing}}}\right)^2\right]$		Captures a single T-peak with *minimal* experimental effort.
$k(T,\sigma) = k(T)\exp\left[const\cdot\sigma^2\right]$		Practical for near-fixed, low–moderate stress fields.
$k(T,\sigma) = k(T)\exp\left[\sum_i const_i\cdot\sigma^2\right]$		Multimode/polydisperse tuning without adding separate FIC submodels.
$\frac{d\theta}{dt} = k\theta^n(1-\theta)$	(19)	Conveniently couples with the energy equations. Close to Avrami without an explicit time dependence
$K = K_q\exp\left[const\cdot N_{11}^{const}\right]$ $\left(K \xrightarrow{\text{Equation (15)}} G\right)$	(20)	Modified quiescent kinetics; good when FIC acts mainly via stress amplification.
$K = K_q\exp\left[\sum_i const_i\cdot N_{11}^{const_i}\right]$		Easier to tune than single-exponent forms; no explicit $\dot{N}$ and/or G model needed.
$N_{11} = \sigma_{xx} - \sigma_{yy} \approx \eta\,\partial V/\partial x$ (1D steady)		Suits prolonged uniaxial elongation (e.g., spinning) with known $V(x)$.
$\eta_e(T,\chi) = \eta_e(T)\cdot\exp\left(const\cdot\chi^{const}\right)$	(21)	Embeds FIC via η; adequate when relative crystallinity control is sufficient.
$\eta_e(T,\chi) = \eta_e(T)\,(1+const\cdot\chi)$		Useful for simplified spinning; no CFD mesh needed for $\chi(T)$.
$\eta_e(T,\chi) = \eta_e(T)\,(1-\chi)^{-const}$		May be stiff at high cooling rates; monitor stability.
$\eta_e(T,\theta) = 3\eta(T)\cdot f(const\cdot\theta)$	(22)	Handles complex external forcing (e.g., spunbonding) via a calibrated f.
$\Delta\mathbb{G}_f = const_{\text{Fold}}\cdot const_{\text{Surface}}\cdot const_{\Delta H}\cdot\Delta\mathbb{G}_q$	(23)	Useful to estimate shifts in effective T_c without full MD.
Machine learning algorithms	-	They are useful when operating the process is available to provide an abundance of data.

Type 1 models are simple to implement, add a few transport couplings, and reduce divergence risk. They are fast for single- or multi-phase polymers but do not capture full multidimensional effects and require informed supervision for validity.

3.2. Type 2: Avrami with a Flow Correlation

Type 2 methods upgrade Type 1 by coupling Avrami kinetics with an additional, semi-empirical flow correlation. The add-on introduces specific FIC physics into the transport set by targeting one or more of T_c, G, or $\dot{N}$ [87]. This increases the number of $const$s and the experimental burden, but typically yields higher accuracy and enables more than one spatial dimension in applied studies [34,113,114]. Because strain distributions differ across a cross-section versus along the flow, 2D implementations often include shear-related contributions within kinetics (e.g., through Equations (11) and (14)) while remaining compatible with CFD transport equations.

3.2.1. Elevating the Effective T_c

Building on observations that flow can initiate crystallization above the quiescent T_c and, in certain cases, even above T_m [115], Haas and Maxwell [116] proposed

$$\begin{aligned} T_c &= T_c^q\left(1+\frac{\tau^2}{2\,\Delta H\cdot G_{\text{Kirchhoff}}}\right) \qquad \text{(quiescent } T_c^q \text{ elevated by shear stress } \tau\text{)} \\ G_{\text{Kirchhoff}} &= \frac{\rho R T_c}{M_e} \qquad \text{(estimate via density } \rho\text{, } R\text{, and entanglement molecular weight } M_e\text{)} \end{aligned} \tag{24}$$

where chain orientation reduces configurational entropy S and thereby free energy $\mathbb{G} = H - TS$, facilitating earlier onset. Guo and Narh [117] emphasized contributions from strain rate, strain time, and stress relaxation, adopting an empirical Godovsky–Slonimsky-type fit:

$$\begin{aligned} \Delta T_c = T_c - T_c^q \;&=\; const\cdot\exp\left(\frac{const}{\tau}\right) \qquad \text{(valid within the experimental fitting range)} \\ \text{with } \theta:\ &\text{Equation (3)}, \quad t_{ind}:\ \text{Equation (4)}. \end{aligned} \tag{25}$$

Kim and Kwon [118] embedded the elevated T_c as a function of stress in HL (Equation (15)) and advanced Avrami in a 2D injection-molding CFD, resolving strong skin-layer shear and recommending region-specific $const$ tuning. Limitations include insensitivity to polydispersity and possible shifts in enthalpy under flow and

cross-linking [29], which motivate additional adjustments when needed. Zhou et al. [66] similarly refined $t_{1/2}$ (in HL's supercooling term) via two empirical relations (six $const$s), linking temperature and dissipation to G.

3.2.2. Stress-Assisted Nucleation and Rate Amplification

Coupling can also proceed by assuming G and ΔT_c are T-driven while flow primarily augments nucleation ($N = N_q + N_f$). Ziabicki et al. [119] proposed a spinning-oriented model in which N_{11} governs both K and $\dot{N}_f$:

$$\begin{aligned} K(T, N_{11}) &= K_q \cdot \exp\left[\frac{-4\ln(2)\cdot(T - T_{\text{ref}})}{\Delta T_{1/2}^2} \;+\; const \cdot \left(\frac{N_{11}}{N_{1\text{-ref}}}\right)^2\right] \\ \dot{N}_f &= const \cdot N_{11} \qquad N_{11} = \sigma_{zz} - \sigma_{rr} \quad \text{(axial } z\text{, radial } r \text{ for spinning)} \end{aligned} \tag{26}$$

Here the reference ratio $N_{11}/N_{1\text{-ref}}$ can be related to a birefringence (rheo-optical) ratio $\Delta m/\Delta m_{\text{ref}}$, indicating the fraction of aligned chain segments. Because the cooling region is inherently multidimensional, 2D approximations are often preferred for robustness and experimental comparability.

Tanner and Qi [120] introduced a convolution-type contribution of flow-activated nuclei alongside quiescent Avrami,

$$\begin{aligned} \theta &= 1 - \exp\left[-\left(k\,t^n \;+\; const \cdot \int_0^t \dot{N}_f (t-s)^n \, ds\right)\right] \\ \dot{N}_f &= const \cdot \exp\left[-\tfrac{t}{f(\lambda)}\right] \qquad \text{(relaxation-controlled activation; } f \text{ empirical in } \lambda) \end{aligned} \tag{27}$$

and, using HL for growth (Equation (15)), identified a minimum strain threshold (via f) to activate extra nucleation. Derakhshandeh et al. [77] broadened validation for both shear and elongation.

Rong et al. [121] formulated an Avrami-consistent expression that separates pre-existing, shear-activated (of duration t_s), and time-integrated nucleation:

$$\begin{aligned} k\,t^n &= const_1 \cdot G(T)^n \left[\, N_q\, t^n \;+\; N_f\,(t - t_s)^n \;+\; \int_0^{t_s} \dot{N}_f(s)\,(t-s)^n \, ds \,\right] \\ N_q &= \exp\big(const \cdot \Delta T + const\big) \qquad \text{(temperature-driven pre-existing nuclei)} \\ \dot{N}_f &= const \cdot N_{11} \quad \Rightarrow \quad N_f = \int \dot{N}_f \, dt \qquad \text{(flow-assisted nucleation via } N_{11}) \end{aligned} \tag{28}$$

This decouples T-controlled growth from N_{11}-controlled nucleation, enabling finer spatial resolution of θ than temperature-only fits.

3.2.3. Free-Energy Formulations and Viscoelastic Context

Zheng et al. [81,122] modeled stress effects by splitting free energy $\mathbb{G} = \mathbb{G}_q + \mathbb{G}_f$, with empirical closures:

$$\begin{aligned} N_q &= \exp[const \cdot \Delta T + const] \;=\; f_1(\mathbb{G}_q, t_{1/2}) \quad \left[\tfrac{\text{number}}{\text{volume}}\right] \\ \mathbb{G}_f &= const \cdot f_2(2\,Wi) \qquad (f_2\text{: empirical function of } Wi) \\ \dot{N}_f + \frac{N_f}{const} &\;=\; f_3(\mathbb{G}) \qquad (f_3\text{: empirical function of total } \mathbb{G}) \end{aligned} \tag{29}$$

The Weissenberg number captures stretch severity (and thresholds Wi_{rept}, Wi_{Rouse}); empirical f_i require substantial calibration.

Within a viscoelastic framework, Doi–Edwards (DE) provides a more analytical bridge than Wi alone [78,79,123]. Marrucci and Grizzuti [46] expressed a deformation-dependent free energy contribution and proposed nucleation kinetics for shear/elongation:

$$
\begin{aligned}
&\mathbb{G} = \mathbb{G}_f(De) + \mathbb{G}_q(T) \qquad \text{(see [46] for explicit forms)} \\
&\mathbb{G}_q = \Delta H_q \left(1 - \frac{T}{T_c^q}\right) \\
&\dot{N} = const \cdot T \cdot \mathbb{G} \cdot \exp\left(\frac{const}{T}\right) \cdot \exp\left(\frac{const}{T\,\mathbb{G}^{\,const_1}}\right) \\
&\dot{N} \propto t_{\text{ind}} \qquad const_1 = 1 \text{ or } 2
\end{aligned}
\tag{30}
$$

Acierno and Maffettone [124] validated the shear case against rheometry; we are not aware of an elongational $\mathbb{G}_f$ application published for this specific form. Note the TF-like structure (Equation (13)) in $\dot{N}$'s temperature dependence.

It should be noted that the empirical correlations employed in Type 1 and 2 models are often calibrated for specific polymers, flow conditions, and thermal histories. As a result, the transferability of fitted parameters across materials and processing regimes is limited, and associated uncertainties may propagate into CFD predictions. While these simplified formulations are attractive for their numerical efficiency, their applicability should be critically assessed when extrapolated beyond the experimental conditions used for parameter identification. It has also been reported that geometric complexity significantly affects FIC [125], which can limit the applicability of Type 1 and 2 models even in moderately twisted two-dimensional geometries.

3.2.4. When to Choose Type 2

Adding empirical coefficients can represent multiple growth regimes (e.g., [65]) and deliver process-specific accuracy when experimentation is feasible. Without such resources, fewer *const*s are preferable, since fitted values can drift with grade or operating window. Because many Type 2 variants still rely on empirical adjustments, a practical question remains: is the added experimental and computational cost justified over Type 1 for your design objective? In our experience, Type 2 is best for detailed process analysis and optimization once a baseline process is known. Table 6 provides a summary of the corresponding models.

Table 6. Pros and cons of Type 2 models.

Type 2 Model	Equation	Comments
$\Delta T_c = const \cdot \exp\left(\frac{const}{\tau}\right)$	(25)	Elevates T_c with minimal *const*s; empirical fit valid over a measured stress range; not chain-length aware.
$K(T, N_{11}) = K_q \exp\left[\frac{-4\ln(2)(T-T_{\text{ref}})}{\Delta T_{1/2}^2} + const\left(\frac{N_{11}}{N_{1\text{-ref}}}\right)^2\right]$	(26)	Low experimental burden; effective for uniaxial FIC (e.g., spinning); relies on birefringence or stress proxy.
$\theta = 1 - \exp\left[-\left(kt^n + const\int_0^t \dot{N}_f(t-s)^n ds\right)\right]$	(27)	Generalizable; needs several experiments; suitable for low-crystallinity, spherulitic growth under modest flow.
$kt^n \propto G(T)^n\left[N_q t^n + N_f(t-t_s)^n + \int_0^{t_s} \dot{N}_f(s)(t-s)^n ds\right]$	(28)	Extends the above; decouples T-driven G from N_{11}-driven nucleation; useful for blends/precursors.
$\dot{N}_f + \frac{N_f}{const} = f_3(\mathbb{G})$ (with $\mathbb{G}_f \sim f_2(Wi)$)	(29)	Free-energy route; flexible but calibration-heavy (empirical f_i); interpretable via Wi thresholds.
$\mathbb{G} = \mathbb{G}_f(De) + \mathbb{G}_q(T)$	(30)	Captures FIC severity via De; t_{ind} handling matters; simpler experiments but more complex coding.

Type 2 improves accuracy at the expense of extra *const*s and measurements. With adequate lab support (DSC, birefringence, rheometry, WAXS), it predicts large-scale structure well across processes. Caution: forcing Avrami forms deep into high-flow regimes may be problematic without regime-aware modifications.

3.3. Type 3: Analytical Approach with the Stress Tensor

Type 3 targets a fuller, stress–aware description of FIC by solving for the stress tensor, $\underline{\sigma}$, over the domain with minimal empirical adjustments. Compared to Type 2, it leverages viscoelastic rheology to capture coupled shear–elongation effects for process design, not only analysis. As a result, Type 3 typically supplies explicit correlations for $\dot{N}$, G, and/or ΔT_c, and is more computationally demanding. Representative solvers that can host such models and FIC add-ons include Ansys Polyflow [126], viscoelasticFluidFoam [15], rheoTool [33,127], and

LBFoam [128,129]. In some cases, inputs at chain/monomer scale are required.

A defining feature of Type 3 is the explicit use of the stress tensor with rheology that treats elongation and shear concurrently. This realism raises numerical stiffness; many applied studies therefore reuse elongational FIC forms developed for shear (as in Type 2) while solving a viscoelastic momentum set.

A common first step distinguishes elongational from shear viscosity via a Newtonian or linear viscoelastic envelope (LVE):

$$\begin{aligned} \eta_e &= 3\eta && \text{Newtonian} \\ \eta_e &= 3\eta\left[1-\exp\left(\frac{-t}{\lambda}\right)\right] && \text{LVE} \end{aligned} \tag{31}$$

where η is the shear viscosity on the zr-plane (perpendicular to the spinline). Although elongational FIC is typically stronger than shear [130], this simplification is often adequate for moderate flows in regimes II and (parts of) IV [131] of Figure 6.

3.3.1. Doufas-McHugh Framework

Doufas and McHugh pioneered Type 3 by coupling a viscoelastic stress field with FIC kinetics. In [132], they formulated dimensionless free-energy and rheology for elongational FIC (Giesekus melt; multi-bead crystallites), and later applied it to MS [133]:

$$\begin{aligned} \frac{D\theta}{Dt} &= nk[-\ln(1-\theta)]^{(n-1)/n}(1-\theta)\cdot\exp\left[f\left(\frac{\mathbf{tr}\underline{\sigma}}{G_{\text{Kirchhoff}}}\right)\right] \\ \underline{\sigma} &= \underline{\sigma}_{\text{amorph}}+\underline{\sigma}_{\text{crystal}} \qquad k \text{ from Equation (18)} \end{aligned} \tag{32}$$

The first line is a material-derivative form of Avrami with a stress-dependent amplification; **tr** is the matrix trace and f is empirical. The second line couples amorphous and crystalline stress contributions. Chains exit the die with M_0 [number of] average springs of length l; as crystallization progresses, springs convert to rigid segments (Kuhn view [134]), stiffening the chain. They defined

$$\begin{aligned} \theta &= 1-\frac{M}{M_0} && \text{(fractional conversion of springs)} \\ K_{\text{spring}} &= \frac{3k_BT}{N(1-\theta)^2l} && \text{(effective spring constant)} \end{aligned} \tag{33}$$

with k_B the Boltzmann constant and M the instantaneous average number of springs (microstructural segments). In thin-fiber spinning they simplified Equation (2) (no ΔT_c elevation; negligible t_{ind}), so T follows convection plus sensible/latent heat; θ, M, and K_{spring} then vary mainly along the spinline x in steady state. Two conformation tensors were introduced: one for amorphous stretch (depending on k_B, T, K_{spring}, λ_{amorph}) and one for crystal alignment (depending on T, θ, λ_{crystal}, and U). The model predicts both the onset x_{onset} and freezing $x(\theta\approx1)$. Later work [135] combined HL (Equation (15)) to determine k, and was validated on additional materials (PLA, etc.) with tuning [136–138].

Dhadwal [139] extended Doufas to MS and introduced a spherulitic link:

$$\begin{aligned} k &= k_{1/2}\left(\frac{4\pi}{3}\cdot\frac{N_q}{\chi_\infty}\right)^{1/3}\cdot\exp\left[-\left(\frac{T-T_{1/2}}{T_c-T_{\text{freezing}}}\right)^2\right] \\ N_q &= 10^{10}\quad\frac{\text{Nuclei}}{cm^3} \end{aligned} \tag{34}$$

where the numeric N_q is a material/grade-specific calibration.

3.3.2. Dual-Scale Coupling: Spina & Spekowius

Spina, Spekowius, and collaborators [80,140,141] combined a macroscale FVM (Avrami, HL, Haas–Maxwell) with a microscale FEM (Acierno/Maffettone) via SphäroSim [142]:

$$\begin{aligned} &\text{Macroscale} && \to\theta: \text{Equation}(9) \quad k: \text{Equation}(15) \quad T_c: \text{Equation}(24) && \text{FVM: melt in air} \\ &\text{Microscale} && \to\dot{N}: \text{Equation}(13) \quad G: \text{Equation}(15) && \text{FEM: crystals in melt} \\ &\text{Rheology} && \to\eta(T)=\eta_{\text{ref}}\exp\left(\frac{-E_D}{RT}\right)+\text{Cross-WLF} && \text{Generalized Newtonian} \end{aligned} \tag{35}$$

Their probabilistic Monte Carlo growth accounts for blocking/impingement in 3D.

3.3.3. Shish-Kebab Morphologies: Roozemond et al.

Roozemond et al. [143] modeled pipe-flow shish–kebab by separating spherulitic backbone (sph), parent lamellae (p), and daughter crystals (d), with macro-rate terms (Table 7). Precursors larger than l_{critical} activate at lower T, while flow can stretch shorter precursors l at rate $\dot{l}$ until $l + \dot{l}t > l_{\text{critical}}$. Shish grows along the flow but may still be represented by spherulitic-type k-terms:

Table 7. Roozemond mathematical models

Equations		Explanation
$l_{\text{critical}} = \dfrac{s}{\Delta H\left(1 - \frac{T}{T_m}\right)}$	Quiescent	Starting from Schneider's ODE framework (Equation (14)), s is the surface energy; $\mathbb{G}_{\text{volume}}$, $\mathbb{G}_{\text{side}}$, and $\mathbb{G}_{\text{end}}$ are bulk/side/end surface free-energy contributions of a cylindrical precursor. The radius change $\dot{R}$ captures specific shish growth; phase competition between p and d may arise [144]. Λ measures average backbone stretch from $\underline{C}$; **tr** mixes shear and elongation.
$N_q = const \cdot \exp\left[-const \cdot (T - T_{\text{ref}})\right]$		
$\dot{N}_{\text{total}} = \dot{N}_q \cdot \exp\left[const \cdot (\Lambda^2 - 1)\right]$	FIC	
$\mathbb{G}(l) = -\mathbb{G}_{\text{volume}} + \mathbb{G}_{\text{side}} + \mathbb{G}_{\text{end}}$	Shish	
$\Lambda = \sqrt{(\mathbf{tr}\underline{C}/3)} \cdot (\Lambda^2 - 1)]$		
Three morphologies in distinct flow regions [145]: 1. sph: a central backbone (fibrillar shish) growing along the flow, 2. p: parent lamellae (kebab) growing radially, 3. d: daughter crystals at boundaries, growing on kebab surfaces.		
$k_{sph} = \dfrac{4\pi}{3}\dot{N}_{\text{total}} G_{\text{sph}}^3$ or Equation (5)	$G_{sph}(T) \cdot const_{sph} \cdot \exp\left[-const_{sph}(T - T_{\text{ref}})^2\right]$	Quiescent
$k_p = 2\pi\dot{R}\dot{G}_p^2; \quad w_p = \dfrac{G_p}{G_p + G_d}$	$G_d(T) \cdot const_d \cdot \exp\left[-const_d(T - T_{\text{ref}})^2\right]$	Quiescent
$k_d = 2\pi\dot{R}\dot{G}_p\dot{G}_d; \quad w_d = 1 - w_p$	$G_p(t,T) = G_q(T)\left[1 + const \cdot \exp\left(-t/\lambda\right)\right]$ Parallel Avrami terms applied per morphology.	FIC
$\theta = 1 - \exp\left(-t[k_{sph} + w_p k_p + w_d k_d]\right)$		

3.3.4. 3D Deposition and Recent Extensions

Yarin–Pourdeyhimi's group ported Types 1–2 elements into 3D fiber deposition with elongational stress and deposition kinetics [146,147]:

$$\begin{aligned} &\dot{N} : \text{Equation (30)} \\ &\eta = const \cdot \exp\left[\frac{E_D}{RT}\right] \cdot \exp\left[const \cdot \chi^{const}\right] \qquad \text{As in Equation (21)} \\ &T_m = T_m^q \cdot const^{\text{correlation}} \\ &\theta = 1 - \exp\left[A \int_0^t G(v) \cdot \left(\int_0^s \dot{N}(u) \cdot du\right) \cdot dv\right] \quad \text{(cylindrical)} \end{aligned} \tag{36}$$

Later, for spunbonding [148], they included relaxation time, airflow, and an upper-convected Maxwell model in Lagrangian coordinates, refining over multiple works [149–152]. Santoro et al. [153] combined t_{ind} (Equation (4)) with Kim et al. [118] (Type 2), i.e., Nakamura (Equation (9)) + HL (Equation (15)) with ΔT_m from Haas–Maxwell (Equation (24)), tuning nine $const$s.

Saad et al. [154] proposed an Ozawa-inspired (β, Equation (12)) 3D form with deformation-rate coupling:

$$\begin{aligned} &\frac{D\theta}{Dt} = (1 - \theta)\left[-\frac{1}{\beta}\frac{\partial \eta}{\partial \theta}\mathbf{tr}\underline{D}^2 + nK(T)^{1/n}(-\ln(1 - \theta))^{1-1/n}\right] \\ &G : \text{Equation (15)} \qquad T_m(p) = T_m^q + const \cdot p \qquad T_g(p) = T_g^q + const \cdot p \end{aligned} \tag{37}$$

This incorporates $\underline{D}$ to treat shear and elongation simultaneously in 3D, employs Cross–WLF rheology, and includes pressure effects p, using six $const$s overall. Despite local p deviations, the framework is practical for complex molds.

3.3.5. State-of-the-Art with Conformation Dynamics (Peters et al.)

Peters and coworkers developed XPP-based flow–structure models for injection molding [155], relating entanglement count Z to λ thresholds (Figure 3) and coupling conformation to nucleation/growth:

$$
\begin{aligned}
&\dot{N}_q = const \cdot \exp\left(-const[T - T_{\text{ref}}]\right) && T \text{ dependence [156]}\\
&\dot{N}_{q,i} = \frac{G_i}{\sum G_i}\frac{dN_q}{dT}\dot{T} && \text{Multi-mod}\\
&\dot{N}_f = f(T - T_{\text{ref}}, \underline{\sigma}) && \text{Function chain stretch}\\
&\nabla \underline{C}_i + \frac{2\exp\left[const_1 \cdot (\Lambda_i - 1)\right]}{\lambda_{\text{Rouse}}} \cdot \left(1 - \frac{3}{\mathbf{tr}\underline{C}_i}\right) \cdot \underline{C}_i + \frac{1}{\lambda_{\text{orient}}} \cdot \left(\frac{3\underline{C}_i}{\mathbf{tr}\underline{C}_i} - I\right) = 0 && \text{Conformation}\\
&\underline{\sigma} = \sum_i \frac{\eta_i}{\lambda_i}(\underline{C}_i - I) \qquad \Lambda = \sqrt{\frac{\mathbf{tr}\underline{C}}{3}} && \text{XPP}\\
&\dot{N}_f = f(T) \cdot \exp\left[const \cdot (\Lambda^2 - 1)\right] \qquad \text{Shish grows with nucleation along stretch} && \dot{N}_f(\underline{C})\\
&G_i = G_{i,max} \cdot \exp\left[const_i \cdot (T - T_{\text{ref}})^2\right] \qquad i: \text{3 growth modes in Table 7} && [157]\\
&\dot{l}_{\text{shish}} = 2N_f\sqrt{3}\dot{\varepsilon} \qquad \text{Other phases grow with affine motion}\\
&\dot{\varepsilon} = \sqrt{\frac{2}{3}\underline{D} : \underline{D}} && \text{LVM}\\
&t_{ind} \propto \frac{1}{\dot{\varepsilon}} \text{ or } t_{ind} = \text{Equation}(4) && [47]
\end{aligned}
\tag{38}
$$

with mode index i, λ_{Rouse} (backbone stretch) and λ_{orient} (orientation) relaxations, and I the identity. They captured near-wall FIC structures [68,93] and the regime-dependent transitions [31,60,94,155]. The conformation measure $\Lambda = \sqrt{\mathbf{tr}\,\underline{C}/3}$ correlates with critical thresholds observed in shish micrographs and rationalizes strain hardening via oriented lamellae transverse to load.

Type 3 delivers higher physical fidelity at the cost of complexity, solver modification, and extensive calibration for transfer across processes/grades. Many comprehensive studies still collapse crystallization to temperature-driven χ when numerics become prohibitive. For high accuracy, Type 3 benefits from mesoscale inputs (e.g., shish growth rates, Kuhn-statistics) and carefully designed validation (WAXS, birefringence, rheometry). We summarized the selected models of Type 3 in Table 8.

Table 8. Pros and cons of Type 3 models.

Type 3 Model	Equation	Comments
$\frac{D\theta}{Dt} = nk[-\ln(1-\theta)]^{(n-1)/n}(1-\theta)\cdot\exp\left[f\left(\frac{\mathbf{tr}\underline{\sigma}}{}\right)\right]$	(32)	Stress-coupled Avrami; requires viscoelastic stress and careful stabilization. Good for thin spinline flows.
$\theta = 1 - \exp\left(-t[k_{sph} + w_p k_p + w_d k_d]\right)$ (Table 7)	(14)	Schneider-ODE backbone with morphology-specific rates; many tunables but physically interpretable; stable numerically when calibrated.
$G_i = G_{i,max}\exp\left[const_i(T - T_{\text{ref}})^2\right]$	(38)	Conformation/XPP-driven nucleation + multi-mode growth; accurate and modern, heavier setup and calibration.
$\theta = 1 - \exp\left[A\int_0^t G(v)\left(\int_0^s \dot{N}(u)\,du\right)dv\right]$	(36)	Type 2 structure embedded in 3D deposition; practical for spinning/deposition with measured T_m shifts.
$\frac{D\theta}{Dt} = (1-\theta)\left[-\frac{1}{\beta}\frac{\partial\eta}{\partial\theta}\mathbf{tr}\underline{D}^2 + nK(T)^{1/n}(-\ln(1-\theta))^{1-1/n}\right]$	(37)	3D coupling (shear+elongation), Cross–WLF, pressure effects; good overall performance in complex molds.

Type 3 resembles molecular FIC at a continuum level. It fits FEM/FVM but carries numerical risk due to many coupled fields. Best for research/advanced design with strong experimental support (WAXS, birefringence, rheometry). Early variants blur shear/elongation; later ones introduce conformation dynamics to address regime changes.

3.4. Type 4: Molecular and Mesoscale Dynamics

Up to this point, we have treated the polymeric melt as a continuum of solidifying fluid described by bulk variables such as θ, T, G, and M. These domain-averaged quantities are powerful but can miss sub-continuum phenomena (e.g., cross-linking, precursor activation, nascent nuclei). Type 4 instead models chains as discrete

objects (monomers, Kuhn segments, or coarse-grained beads), providing access to microscopic mechanisms—most importantly $\dot{N}$—that are not directly resolvable with macroscopic thermodynamic/transport equations.

In this approach, one or several chains are represented as in Figure 6b: uniaxial stiff springs (UAs) store/release energy as chains entangle/untangle, and a nucleus activates near stems where several Kuhn segments align within a limited volume [158,159]. Molecular dynamics (MD) can be used directly, or adapted in spirit to the DE framework, to interrogate entanglement under strain, chain folding, melt squeezing, cold crystallization, and relaxation at chain/segment/monomer scales. Whether simulating individual molecules or coarse-grained particle ensembles, MD provides a route to understanding FIC at the scale where it initiates.

At the mesoscale, crystallization can also be represented using empirically tuned parameters, in analogy with Type 1 and Type 2 approaches. This strategy has been applied to model multiphase crystallization of nanofibers within spunbonded fibers [160], where elongational forces vary significantly along the spinline [161].

Two broad strategies are common: (i) single-chain or few-chain simulations, and (ii) statistical/stochastic analyses of many small-scale events, often within a dual-scale (micro–macro) pipeline. Because thermodynamic variables (e.g., T) are bulk, a microscopic indicator for FIC must be defined. Typical choices are:

1. **Contour alignment (Hermans factor)** P_2 [162], with a user-defined activation threshold:

$$P_2 = \frac{3}{2}\left\langle (\vec{e}_i \cdot \vec{e}_j)^2 \right\rangle - \frac{1}{2} \qquad (39)$$
$$P_2 \to 1 : \text{Perfect alignment} \qquad P_2 \to 0 : \text{Random alignment}$$

   where $\vec{e}_i$ and $\vec{e}_j$ are segmental unit vectors (Figure 3b), and $\langle\cdot\rangle$ denotes an ensemble average. An analogous $P_{2,K}$ is used when Kuhn segments are the primitive units.
2. **Local free-energy drop** as a nucleation trigger:

$$\Delta\mathbb{G}_{\text{crystallization}} = f(\Delta\mathbb{G}_{\text{barrier}},\ \text{No. segments aligned},\ \text{No. critical segments}) \qquad (40)$$

In both routes, a threshold is selected (experimentally informed or protocol-based). The segment size remains a hyperparameter chosen to match the scope. Flow is typically imposed with periodic boundary conditions. We summarized the Type 4 information in Table 9.

Table 9. Scales of particles in Type 4 simulation

Scale	Capabilities	Ignoring	Packages
Molecular	P_2, reptation, Rouse, isomerization, t_{ind}, transient FIC, ideal boundaries	Broad molecular mass distribution, bulk T, undercooling fields	LAMMPS [163]
Kuhn	$P_{2,K}$, reptation, Rouse, t_{ind}, local $\Delta\mathbb{G}$, constitutive-chain updates, transient FIC	Sub-Kuhn monomers, absolute T fields	polySTRAND [164] (dual-scale)
Meso	Multi-bead chains, Monte Carlo growth, local $\Delta\mathbb{G}$	Explicit reptation/Rouse details	GO [165], UEF [166], GLaMM [167]
Continuum	Thermodynamics (e.g., T), particle tracking, secondary phases, heterogeneous $\dot{N}$	Polydispersity, reptation/Rouse detail, local entropy	rheoTool [35], SphäroSim [140]
Best Suited for		**Strengths**	**Caveats**
Nucleation physics ($\dot{N}$), precursor statistics, nano/micro features, blend additives		Direct access to chain alignment, local $\Delta\mathbb{G}$, reptation/Rouse, t_{ind}; clarifies regime transitions	Small domains; idealized BCs; expensive; requires thresholds (alignment or energy); careful coarse-graining
Dual-scale coupling to CFD		Supplies informed closures for Type 2 & 3 ($\dot{N}$, G, T_c shifts)	Calibration still required; mapping micro → macro is non-unique
Post-processing on Type 1–3 fields		Robust for nano-fibrils or dispersed phases without re-solving full transport	Limited back-coupling to continuum; assumes weak feedback on flow/thermal fields

A complementary non-equilibrium thermodynamic path builds $\Delta\mathbb{G}$ from conformation/orientation entropy and structural enthalpy changes under flow, with polydispersity effects. Recent work by Li, Nie, Wang, and coworkers [17,24,111,112] shows that long chains tend to act as nuclei under stretch, while short chains preferentially

grow on them, yielding a mesoscale bridge to large-scale correlations such as Equation (23). Their comprehensive review [29] summarizes these multi-scale links; we refer the reader there for details.

Classic molecular studies include Koyama et al. [168], Yamamoto [13], Luo et al. [169], and Sigalas et al. [170]. Graham [20] provides an accessible MD overview, including approaches to quantify $\dot{N}$ in entangled flows and computational limits.

Type 4 has also proven valuable for modern blends and dispersed phases. Our recent in-situ fibrillation work [171, 172] indicates that, at this scale, the experimental–simulation gap narrows: particle tracking tools (e.g., our rheoFibrillator [160, 173]) avoid the need to solve fully coupled transport equations and thus reduce numerical instability. In practice, MD excels with idealized boundaries (periodic, fixed T or U), whereas complex, spatially varying process conditions remain more naturally handled by CFD.

NEMD implementations in LAMMPS [163] can report local energy, UA states, chain stretch, and De thresholds [166]. Read et al. [164] further derived statistical-entropy correlations for nucleation via counting crystal-stem arrangements and segment distributions, reproducing the four FIC regimes. Many of these packages are open-source.

Overall, Type 4 is most compelling when the target phenomenon lives at (or is controlled by) the chain/segment scale—e.g., low-dosage blend morphology, precursor activation statistics, or nano-fibril formation. In such cases, MD (possibly as a post-processor atop Types 1–3) captures scale-separated effects that would be inaccessible or unstable in a fully coupled continuum model.

4. Conclusions

From a thermal-science perspective, the selection of an FIC model directly influences predicted temperature fields through latent heat release, temperature-dependent viscosity, and thermo–rheological coupling.

FIC couples kinematics, rheology, heat transfer, and phase change, making its mathematical formulation complex and still evolving. This review surveyed the principal correlations used for elongational FIC and organized the literature into four model types (Table 4), each progressively incorporating more physics and numerical depth for different simulation scopes.

Section 3 traced the evolution in complexity and highlighted the assumptions that distinguish these types. Table 10 summarizes selected studies chronologically and lists their rheological, momentum, and energy formulations to show the degree of physical simplification. Together, these references form a guide for selecting a model consistent with the desired fidelity and project scope.

In practice, highly detailed models that perform well for idealized or small-scale cases rarely transfer directly to complex industrial geometries; simplifications become inevitable. Accurate FIC modeling in such systems usually requires including at least one transport term among G, $\dot{N}$, or ΔT_c. Each inclusion increases the number of transport equations, empirical coefficients, and computational stiffness. While additional $const$s introduce more physical fidelity, they reduce robustness to variations in feedstock and operating conditions. Consequently, model selection should balance available experimental data, computational stability, and the accuracy required for process design.

Dimensionality and tolerance also influence model choice. When $3D$ spatial precision is critical—such as in additive manufacturing—a Type 3 framework becomes indispensable. For transient or lower-dimensional processes (e.g., injection molding), Types 1 and 2 remain the most efficient compromise between stability and accuracy. Type 4 is best reserved for nano- or micro-scale applications (e.g., electro-spinning, fibrillation) where chain-scale physics dominate and continuum approximations fail.

We suggest a practical four-step guideline for choosing the appropriate FIC type and summarize the recommendations for common polymer processes in Table 11.

(i) The first consideration is throughput and data availability. When material data are scarce or uncertain, Types 1 and 2 minimize the need for extensive calibration and remain practical for industrial or educational simulations. (ii) The second step is assessing scope and resources: in one-dimensional or simplified transient studies, higher types may be unnecessary. (iii) Third, select a rheological model consistent with the simulation scope. Generalized Newtonian models pair naturally with Types 1–2, whereas complex viscoelastic models justify adopting Type 3. (iv) Finally, the available numerical expertise and tools matter. Type 3 implementation requires advanced handling of viscoelastic transport, conformation tensors, and stabilization. Even with modern solvers such as OpenFOAM, COMSOL, or STAR-CCM+, reliable execution remains a challenge, and most current studies still prioritize the rheology model over the FIC kinetics themselves.

Types 1 through 3 integrate directly with CFD transport and remain the standard choice for applied simulations because they yield the complete flow fields (U, p, T, θ). Type 4 achieves higher crystallization fidelity at small scales but lacks the coupling necessary for large-scale flow prediction.

Table 10. Applied research with Simulation in FIC that we studied. Nicholson and Rutledge [167] provide a similar table focusing on quantitative enhanced nucleation models. Thus, we skip that.

Study [1]	Year	Type	Process	Material	Rheo γ	Rheo ε	Crystallization	FIC	Momentum Terms [2]	Energy Terms [3]	Additional Equation
Hsiung [44]	1991	1	IM	PPP [4]	$\dot{\varepsilon}$ = Arrhenius + $\eta(\dot{\gamma})^2$		Equation (9)	t_{ind} corr.	p, η	c_p, ΔH, η	
Chen [109]	2008	1	SB	PP	Artificial Neural Network (ANN) training on their experimental data					-	-
Zhao [174,175]	2013	1	SB	PP	-	Arrhenious + Equation (21)	Equation (9)	Equation (26)	drag, g	ΔH, h	Equation (26)
Konaganti [38]	2016	1	Die swell	HDPE	-	Suspension, K-BKZ	Equation (18)	Ziabicki Equation (21)	p, η	c_p, ΔH, η	K-BKZ from [176]
Kanai [107]	2017	1	SB	PP	-	$\eta_e = 3\eta_s(T) \cdot \exp(G_K, \chi)$	Quiescent diagram	G_K factor	drag, g	c_p, h	Ziabicki
Grice [177]	2018	1	MB	PP	solid with low $G_{\text{Kirchhoff}}$		Avrami Equation (18)	-	air momentum	-	blower design
Liu [178]	2020	1	$3D$ print	no limit	UM + Equation ([15])		Instantaneous	-	p, η	c_p, ΔH	Voller [179]
Höhnemann [180]	2023	1	SB+MB	PP, ...	-	$f(De, \lambda, p)$	water-like	-	drag, η	c_p	Nanoval Tech.
Haas [116]	1969	2	Observe	PE, PB-1	Experiment		-	$\Delta T_m \propto \tau^2$	-	-	Entropy
Isayev [45,118]	1995–2004	2	IM	iPP	Cross WLF	-	Equation (9)	$\dot{\theta} = (\dot{\gamma}/\dot{\gamma}_{cr})^2(1 - \theta)/\tau - \theta/\tau$	η	β	FIC layer and t_{ind}
Guo [117]	2002	2	Observe	PET, PP	-	-	Equation (9)	$\Delta T_m \propto \tau^2$	-	-	ΔS
Kim [118]	2005	2	IM	iPP	UM + $\eta = const. \exp(const/T)$		HL + Equation (9)	ΔT elevate	p, η	c_p, ΔH , η	$\eta(T, \gamma)$
Zhou [66]	2010	2	IM	PET	WLF	-	HL	$K = f$(dissipation)	p, η, g	c_p, ΔH, η	CFD
Zheng et al. [81]	2010	2	Observe	iPP	Generalized Newtonian, FENE, + suspension		Equation (9),	$\dot{N}_f + \frac{N_f}{\lambda} = f(\mathbb{G})$	-	-	spherulitic, suspension
Rong [121]	2012	2	pipe flow	iPP	FENE-P	-	Equation (9)	$\dot{N}_f = const. N_{11}$	η	-	Stress history
Derakhshandeh [38,77,82]	2012–2016	2	Observe	PE, PP, HDPE	Suspension, K-BKZ	UM	Equation (9)	Tanner and Qi	p, η	ΔH, η	Strain threshold
Doufas [133,135]	1999–2001	3	MS, FM	no limit [5]	$3D$ Gieskus + XPP		Doufas Equation (32)	Doufas Equation (33)	drag, surf, g, η	$c_p \Delta H$, η, h	$\sigma_{amorph} + \sigma_{crystal}$
Acierno [124]	2002	3	Observe	iPP	DE	-	$\Delta G_q + \Delta G_{FIC}$	Marrucci ΔG	-	-	
Kohler [136,137]	2005–2007	3	MS	PLA, PET	$3D$ Gieskus + XPP		Doufas Equation (32)	Doufas Equation 33	drag, surf, g, η	c_p, ΔH, η, h	-
Dhadwal [139]	2011	3	MS	no limit	$2D$ Gieskus + DE		Doufas Equation (32)	Doufas Equation (33)	drag, surf, g, η	$c_p \Delta H$, η, h	Doufas
Ziabicki [119]	2007	3	MS	PET	-	Arrhenius	Equation (9)	Equation (26)	η	c_p	Equation (26)
Spina [80,140,141,181]	2013–2016	3	IM	iPP	Cross-WLF + Arrhenius		Equation (35)	Equation (30) + Monte Carlo	p, η, g	c_p, ΔH, η	Transient, 2-phase
Roozemond [157]	2015	3	Pipe flow	iPP	-	XPP	Parallel Avrami	Table 7	p, η	c_p, ΔH, η	3 morphologies
Pourdeyhimi [146–148,152]	2016–2024	3	MS, SB	PET, PEO	UM + Arrhenius + λ		Equation (36)	Ziabicki	p, drag, g, η	c_p, η, h	Deposition
Peters [61,94,155,156]	2019–2024	3	IM, Spinning	several	XPP & $3Z \cdot Wi_{\text{strect}} = Wi_{\text{Rouse}}$		Schneider Equation (14)	Peters Equation (38)	p, η, $\underline{\sigma}$	c_p, ΔH, η, $\underline{\sigma}$	$t_{ind} \propto \frac{1}{\dot{\varepsilon}}$
Speranza [182,183]	2020–2024	3	IM	PP	WLF		Schneider Equation (14)	Peters Equation (38)	p, η	T	fibrillar $\dot{N}$
Koyama [168]	2002	4	Observe	PE	-	MD	MD	MD	-	-	-
Nicholson [166,167,184]	2016–2019	4	shear & uniaxial	n-n-alkane	DE, λ_{rept}, λ_{Rouse}		$\underline{C}$, P_2, $\Delta\mathbb{G}$		Forced strain	-	LAMMPS
Li [17,24,111]	2006–2024	4	biaxial	PE	uFIC: $\mathbb{G}$ in Equation (23) with MD		$\frac{1}{T_m^f} = \frac{\Delta H}{\Delta H_f T_m^q} - \frac{\Delta S_{\text{conform}} + \Delta S_{\text{orient.}}}{\Delta H}$			POLYdisperse, uFIC, & PolySTRAND [29]	
Battocchio [185]	2017	4	SB	-	$3D$ vibrating solid		DE multi-bead		drag	Work	bending
Khomami [88,89,186,187]	2020–2023	4	uni & biaxial	PE	DE, λ_{rept}, λ_{Rouse}		$\underline{D}$, P_2, $\Delta\mathbb{G}$		Forced strain	-	NEMD, λ derived
Gangal [188]	2024	4	biaxial	PE	DE, λ_{rept}, λ_{Rouse}		$\underline{C}$, P_2, $\Delta\mathbb{G}$		Forced strain	-	NEMD, ends
Hussain [189]	2025	4	uniaxial	HDPE	DE, λ_{rept}, λ_{Rouse}		Equation (39)		Forced strain	-	NEMD, ends

[1] Only one author's names are listed in this short table. [2] We use η: viscous forces, g: gravity, surf: surface tension, and p: pressure field. [3] We use c_p: conductive heat transfer, h: convective heat transfer, ΔH: latent heat of fusion, and η: viscous dissipation. [4] poly (p-phenylene sulfide). [5] They used dimensionless parameters.

Table 11. Recommendations for simulation types applicable to common polymer processes. "Availability" reflects literature coverage, and the final column indicates the additional difficulty of obtaining reliable $const$s for blends.

Process	No. D	Complexity [1]	Availability [2]	Suggestion [3]	Blend [4]
Melt blowing (MB)	2–3D	Severe	Scarce	1 & 2	1
Injection molding (IM)	2–3D [5]	Complex	Moderate	1 & 2	1
Extrusion	2–3D	Moderate	Moderate	1–3	1 & 2
Blow molding (BM)	2–3D	Complex	Rare	1 & 2	1
Melt spinning (MS)	1–2D	Moderate	Moderate	1–3	1 & 2
Spunbonding (SB)	1–2D	Complex	Scarce	1 & 2	1
Film casting	1–2D	Moderate	Moderate	1–3	1 & 2
Thermoforming	2–3D	Moderate	Moderate	1 & 2	1
Rotational molding	1–2D	Moderate	Moderate	1–3	1 & 2
Compression molding	2–3D	Moderate	Moderate	1–2	1
Calendering	1–2D	Moderate	Moderate	1–3	1
Pultrusion	2–3D	Complex	Moderate	1–3	1 & 2
Reactive extrusion	1–2D	Complex	Rare	1 & 2	1
Hot-melt adhesive	1–2D	Complex	Rare	1 & 4	1 & 4
3D printing	1–3D	Complex	Moderate	3 & 4	3 & 4
Electro-spinning	1–2D	Complex	Moderate	2–4	2 & 4
Fiber-in-Fiber	1–2D	Severe	Scarce	case-specific (1 & 4)	1 & 4

[1] Complexity of the base transport equations before adding an FIC model. [2] Approximate density of applicable FIC models in the literature. [3] Suggested type(s) for a pure throughput with known melt data. [4] Increased difficulty when experimental $const$ data are unavailable for blends. [5] "2–3D" indicates that 2D, 2.5D, and 3D are all used in published studies.

For future work, the heavy dependence of G, $\dot{N}$, and ΔT_c on material and process parameters limits the incentive to derive universal forms. Instead, current trends increasingly focus on nucleating agents [76] and multi-phase or fiber-in-fiber structures. Our own recent contributions [171,172,190] show that the simpler formulations of Types 1–2 often suffice for design and analysis when combined with measured calibration. The addition of dispersed phases introduces further variables and continues to inspire active research on additive engineering in polymeric melts (e.g., [191–196]).

Author Contributions

B.M.: conceptualization, methodology, software, Methodology, Visualization, Formal analysis, Writing—original draft; A.S.: Data curation, Methodology; M.K.: Formal analysis, Visualization; A.J.: Writing—review & editing; M.B.: Resources, Software, Project administration; C.P: Resources, Funding acquisition, Writing—review & editing, Project administration. All authors have read and agreed to the published version of the manuscript.

Funding

This work was supported by the Technology Innovation Program (or Industrial Strategic Technology Development Program) (RS-2024-00433288) funded by the Ministry of Trade, Industry & Energy (MOTIE), Korea.

Acknowledgments

We acknowledge using diagrams.net to create the graphics in Figure 2.

Conflicts of Interest

The authors declare no conflict of interest.

Use of AI and AI-Assisted Technologies

During the preparation of this work, the authors used ChatGPT to improve the English writing. After using this tool/service, the authors reviewed and edited the content as needed and take full responsibility for the content of the published article.

References

1. Hosseinnezhad, R.; Vozniak, I.; Morawiec, J.; et al. Evolution of green in-situ generated polyamide nanofibers controlled by viscoelasticity. *Express Polym. Lett.* **2021**, *15*, 250–261.
2. Vozniak, I.; Zaïri, F.; Hosseinnezhad, R.; et al. Design of hybrid PLA/PBS/POM composite based on In-Situ formation of interpenetrating fiber networks. *Compos. Part A Appl. Sci. Manuf.* **2021**, *151*, 106667.

3. Ning, N.; Luo, F.; Pan, B.; et al. Observation of shear-induced hybrid shish kebab in the injection molded bars of linear polyethylene containing inorganic whiskers. *Macromolecules* **2007**, *40*, 8533–8536.
4. Henderson, D.W. Thermal analysis of non-isothermal crystallization kinetics in glass forming liquids. *J. Non-Cryst. Solids* **1979**, *30*, 301–315.
5. Bond, E.B. *Ziegler-Natta and Metallocene-Catalyzed Isotactic Polypropylene: A Comprehensive Investigation and Comparison Using Crystallization Kinetics, Fiber Spinning and Thermal Spunbonding*; The University of Tennessee: Knoxville, TN, USA, 1999.
6. Di Lorenzo, M.; Silvestre, C. Non-isothermal crystallization of polymers. *Prog. Polym. Sci.* **1999**, *24*, 917–950.
7. Mubarak, Y.; Harkin-Jones, E.; Martin, P.; et al. Modeling of non-isothermal crystallization kinetics of isotactic polypropylene. *Polymer* **2001**, *42*, 3171–3182.
8. Ziabicki, A. Polymer crystallization in complex conditions. Towards more realistic modelling of industrial processes. *Macromol. Symp.* **2001**, *175*, 225–238.
9. Cheng, S.Z.; Lotz, B. Enthalpic and entropic origins of nucleation barriers during polymer crystallization: the Hoffman–Lauritzen theory and beyond. *Polymer* **2005**, *46*, 8662–8681.
10. Hu, W.; Frenkel, D. Polymer crystallization driven by anisotropic interactions. In *Interphases and Mesophases in Polymer Crystallization III*; Springer: Berlin/Heidelberg, Germany, 2005; pp. 1–35.
11. Somani, R.H.; Yang, L.; Zhu, L.; et al. Flow-induced shish-kebab precursor structures in entangled polymer melts. *Polymer* **2005**, *46*, 8587–8623.
12. Beyreuther, R.; Brünig, H. *Dynamics of Fibre Formation and Processing: Modelling and Application in Fibre and Textile Industry*; Springer Science & Business Media: Berlin/Heidelberg, Germany, 2006.
13. Yamamoto, T. Computer modeling of polymer crystallization–Toward computer-assisted materials' design. *Polymer* **2009**, *50*, 1975–1985.
14. Hosun, L. A review of spun bond process. *J. Text. Apparel Technol. Manag.* **2010**, *6*, 1–13.
15. Favero, J.L.; Cardozo, N.S.; Secchi, A.R.; et al. Simulation of Free Surface Viscoelastic Fluid Flow Using the viscoelasticInterFoam Solver. In *Computer Aided Chemical Engineering*; Elsevier: Amsterdam, The Netherlands, 2010; Volume 28, pp. 31–36.
16. Zhang, M.C.; Guo, B.H.; Xu, J. A review on polymer crystallization theories. *Crystals* **2016**, *7*, 4.
17. Wang, Z.; Ma, Z.; Li, L. Flow-induced crystallization of polymers: Molecular and thermodynamic considerations. *Macromolecules* **2016**, *49*, 1505–1517.
18. Midha, V.K.; Dakuri, A. Spun bonding Technology and Fabric Properties: a Review. *J. Text. Eng. Fash. Technol.* **2017**, *1*, 126–133.
19. Tang, X.; Chen, W.; Li, L. The Tough Journey of Polymer Crystallization: Battling with Chain Flexibility and Connectivity. *Macromolecules* **2019**, *52*, 3575–3591.
20. Graham, R.S. Understanding flow-induced crystallization in polymers: A perspective on the role of molecular simulations. *J. Rheol.* **2019**, *63*, 203–214.
21. Karatrantos, A.; Composto, R.J.; Winey, K.I.; et al. Modeling of entangled polymer diffusion in melts and nanocomposites: A review. *Polymers* **2019**, *11*, 876.
22. Vyazovkin, S. Activation energies and temperature dependencies of the rates of crystallization and melting of polymers. *Polymers* **2020**, *12*, 1070.
23. Arrigo, R.; Malucelli, G.; Mantia, F.P.L. Effect of the elongational flow on the morphology and properties of polymer systems: a brief review. *Polymers* **2021**, *13*, 3529.
24. Nie, Y.; Wen, J.; Ming, Y.; et al. Mechanisms of Flow-Induced Multistep Structure Evolution in Semicrystalline Polymers Revealed by Molecular Simulations. *Cryst. Growth Des.* **2024**, *24*, 6531–6547.
25. McHugh, A. Mechanisms of flow induced crystallization. *Polym. Eng. Sci.* **1982**, *22*, 15–26.
26. Swartjes, F.H.M. Stress Induced Crystallization in Elongational Flow. Ph.D. Thesis, Technische Universiteit Eindhoven, Eindhoven, The Netherlands, 2001.
27. Janeschitz-Kriegl, H.; Ratajski, E. Some fundamental aspects of the kinetics of flow-induced crystallization of polymers. *Colloid Polym. Sci.* **2010**, *288*, 1525–1537.
28. Lamberti, G. Flow induced crystallisation of polymers. *Chem. Soc. Rev.* **2014**, *43*, 2240–2252.
29. Nie, C.; Peng, F.; Cao, R.; et al. Recent progress in flow-induced polymer crystallization. *J. Polym. Sci.* **2022**, *60*, 3149–3175.
30. Sharaf, M.A.; Kloczkowski, A. Evolution of the Deformation-and Flow-Induced Crystallization and Characterization of the Microstructure of a Single Spherulite, Lamella, and Chain of Isotactic Polypropylene. *Macromol. Chem. Phys.* **2024**, *225*, 2300203.
31. van Meerveld, J.; Peters, G.W.; Hütter, M. Towards a rheological classification of flow induced crystallization experiments of polymer melts. *Rheol. Acta* **2004**, *44*, 119–134.
32. Favero, J.L.; Secchi, A.R.; Cardozo, N.S.M.; et al. Viscoelastic fluid analysis in internal and in free surface flows using the software OpenFOAM. *Comput. Chem. Eng.* **2010**, *34*, 1984–1993.
33. Pimenta, F.; Alves, M. Stabilization of an open-source finite-volume solver for viscoelastic fluid flows. *J. Non-Newton.*

Fluid Mech. **2017**, *239*, 85–104.
34. Tabatabaei, A.; Mark, L.H.; Park, C.B. Visualization of polypropylene crystallites formed from a stressed melt in extrusion. *Polymer* **2016**, *101*, 48–58.
35. RheoTool User Guide. 2024. Available online: https://github.com/fppimenta/rheoTool/blob/master/doc/user_guide.pdf (accessed on 10 August 2024).
36. Khanna, Y.P. Rheological mechanism and overview of nucleated crystallization kinetics. *Macromolecules* **1993**, *26*, 3639–3643.
37. Marrucci, G.; Ianniruberto, G. Interchain pressure effect in extensional flows of entangled polymer melts. *Macromolecules* **2004**, *37*, 3934–3942.
38. Konaganti, V.K.; Derakhshandeh, M.; Ebrahimi, M.; et al. Non-isothermal extrudate swell. *Phys. Fluids* **2016**, *28*.
39. Song, C.; Isayev, A. LCP droplet deformation in fiber spinning of self-reinforced composites. *Polymer* **2001**, *42*, 2611–2619.
40. Mohajer, B.; Salehi, A.; Jalali, A.; et al. A One-Dimensional Model for Polypropylene Fiber Formation in Spunbonding with Cooling Air Boundary. *SSRN* **2024**, SSRN 5004346. http://dx.doi.org/10.2139/ssrn.5004346.
41. Avrami, M. Kinetics of phase change. II transformation-time relations for random distribution of nuclei. *J. Chem. Phys.* **1940**, *8*, 212–224.
42. Godovsky, Y.K.; Slonimsky, G. Kinetics of polymer crystallization from the melt (calorimetric approach). *J. Polym. Sci. Polym. Phys. Ed.* **1974**, *12*, 1053–1080.
43. Hoffman, J.D. The specific heat and degree of crystallinity of polychlorotrifluoroethylene. *J. Am. Chem. Soc.* **1952**, *74*, 1696–1700.
44. Hsiung, C.; Cakmak, M. Computer simulations of crystallinity gradients developed in injection molding of slowly crystallizing polymers. *Polym. Eng. Sci.* **1991**, *31*, 1372–1385.
45. Isayev, A.; Chan, T.; Shimojo, K.; et al. Injection molding of semicrystalline polymers. I. Material characterization. *J. Appl. Polym. Sci.* **1995**, *55*, 807–819.
46. Marrucci, G.; Grizzuti, N. The Free Energy Function of the Doi-Edwards Theory: Analysis of the Instabilities in Stress Relaxation. *J. Rheol.* **1983**, *27*, 433–450.
47. Bischoff White, E.E.; Henning Winter, H.; Rothstein, J.P. Extensional-flow-induced crystallization of isotactic polypropylene. *Rheol. Acta* **2012**, *51*, 303–314.
48. Vyazovkin, S.; Burnham, A.K.; Criado, J.M.; et al. ICTAC Kinetics Committee recommendations for performing kinetic computations on thermal analysis data. *Thermochim. Acta* **2011**, *520*, 1–19.
49. Dimitra, K.; Konstantinos, C. Nonisothermal crystallization kinetics: studying the validity of different Johnson–Mehl–Avrami–Erofeev–Kolmogorov (JMAEK) based equations. *Thermochim. Acta* **2021**, *704*, 179030.
50. Dietz, W. Sphärolithwachstum in polymeren. *Colloid Polym. Sci.* **1981**, *259*, 413–429.
51. Khonakdar, H.A.; Shiri, M.; Asadinezhad, A.; et al. A novel analytical approach to estimate isothermal and dynamic crystallization Avrami kinetic parameters. *e-Polymers* **2008**, *8*, 085.
52. Alms, J.; Hopmann, C.; Wang, J.; et al. Non-isothermal crystallisation kinetics of polypropylene at high cooling rates and comparison to the continuous two-domain pvT model. *Polymers* **2020**, *12*, 1515.
53. Vyazovkin, S.; Sbirrazzuoli, N. Isoconversional analysis of the nonisothermal crystallization of a polymer melt. *Macromol. Rapid Commun.* **2002**, *23*, 766–770.
54. Minale, M.; Carotenuto, C.; Paduano, L.P.; et al. Nonisothermal Crystallization Kinetics of an Ethylene-Vinyl-Acetate: I Calorimetry Versus Rheology. *Polym. Eng. Sci.* **2019**, *59*, 2557–2563.
55. Lambrigger, M. Evaluation of data on the kinetics of isothermal polymer crystallization: Part II. *Polym. Eng. Sci.* **1997**, *37*, 460–462.
56. Nakamura, K.; Watanabe, T.; Amano, T.; et al. Some aspects of nonisothermal crystallization of polymers. III. Crystallization during melt spinning. *J. Appl. Polym. Sci.* **1974**, *18*, 615–623.
57. Ozawa, T. Kinetics of non-isothermal crystallization. *Polymer* **1971**, *12*, 150–158.
58. Turnbull, D.; Fisher, J.C. Rate of nucleation in condensed systems. *J. Chem. Phys.* **1949**, *17*, 71–73.
59. Schneider, W.; Koppl, A.; Berger, J. Non-isothermal crystallization of polymers. System of rate equations. *Int. Polym. Process.* **1988**, *2*, 151–154.
60. Swartjes, F.H.M.; Peters, G.W.; Rastogi, S.; et al. Stress induced crystallization in elongational flow. *Int. Polym. Process.* **2003**, *18*, 53–66.
61. Caelers, H.J.; de Cock, A.; Looijmans, S.F.; et al. An experimentally validated model for quiescent multiphase primary and secondary crystallization phenomena in PP with low content of ethylene comonomer. *Polymer* **2022**, *253*, 124901.
62. Hoffman, J.D.; Davis, G.T.; Lauritzen Jr, J.I. The rate of crystallization of linear polymers with chain folding. In *Treatise on Solid State Chemistry*; Volume 3 Crystalline and Noncrystalline Solids; Springer: Berlin/Heidelberg, Germany, 1976; pp. 497–614.
63. Lauritzen Jr, J.I.; Hoffman, J.D. Theory of formation of polymer crystals with folded chains in dilute solution. *J. Res. Natl. Bur. Stand. Sect. Phys. Chem.* **1960**, *64*, 73.
64. Lamberti, G. A direct way to determine iPP density nucleation from DSC isothermal measurements. *Polym. Bull.* **2004**,

52, 443–449.
65. Velisaris, C.N.; Seferis, J.C. Crystallization kinetics of polyetheretherketone (peek) matrices. *Polym. Eng. Sci.* **1986**, *26*, 1574–1581.
66. Zhou, Y.G.; Shen, C.Y.; Liu, C.T.; et al. Computational modeling and numerical simulation of flow-induced crystallization kinetics during injection molding of polyethylene terephthalate. *J. Reinf. Plast. Compos.* **2010**, *29*, 76–85.
67. Hammami, A.; Spruiell, J.E.; Mehrotra, A.K. Quiescent nonisothermal crystallization kinetics of isotactic polypropylenes. *Polym. Eng. Sci.* **1995**, *35*, 797–804.
68. Schrauwen, B.; Breemen, L.V.; Spoelstra, A.; et al. Structure, deformation, and failure of flow-oriented semicrystalline polymers. *Macromolecules* **2004**, *37*, 8618–8633.
69. Bansal, V.; Shambaugh, R.L. On-Line determination of density and crystallinity during melt spinning. *Polym. Eng. Sci.* **1996**, *36*, 2785–2798.
70. Bansal, V.; Shambaugh, R.L. On-line Determination of Diameter and Temperature during Melt Blowing of Polypropylene. *Ind. Eng. Chem. Res.* **1998**, *37*, 1799–1806.
71. Samon, J.M.; Schultz, J.M.; Hsiao, B.S.; et al Structure development during melt spinning and subsequent annealing of polybutene-1 fibers. *J. Polym. Sci. Part Polym. Phys.* **2000**, *38*, 1872–1882.
72. Mcheik, A.; Mortada, H.; Lakis, H.; et al. Elongational flow-induced crystallization in polypropylene/talc nanocomposites. *Phys. Procedia* **2014**, *55*, 259–264.
73. Tabatabaei, A.; Barzegari, M.R.; Nofar, M.; et al. In-situ visualization of polypropylene crystallization during extrusion. *Polym. Test.* **2014**, *33*, 57–63.
74. Kitoko, V.; Keentok, M.; Tanner, R. Study of shear and elongational flow of solidifying polypropylene melt for low deformation rates. *Korea-Aust. Rheol. J.* **2003**, *15*, 63–73.
75. Chellamuthu, M.; Arora, D.; Winter, H.H.; et al. Extensional flow-induced crystallization of isotactic poly-1-butene using a filament stretching rheometer. *J. Rheol.* **2011**, *55*, 901–920.
76. Acierno, S.; Pasquino, R.; Grizzuti, N. Rheological techniques for the determination of the crystallization kinetics of a polypropylene–EPR copolymer. *J. Therm. Anal. Calorim.* **2009**, *98*, 639–644.
77. Derakhshandeh, M.; Doufas, A.K.; Hatzikiriakos, S.G. Quiescent and shear-induced crystallization of polyprophylenes. *Rheol. Acta* **2014**, *53*, 519–535.
78. Doi, M.; Edwards, S. Dynamics of rod-like macromolecules in concentrated solution. Part 1. *J. Chem. Soc. Faraday Trans. Mol. Chem. Phys.* **1978**, *74*, 560–570.
79. Doi, M.; Edwards, S.F. Dynamics of rod-like macromolecules in concentrated solution. Part 2. *J. Chem. Soc. Faraday Trans. Mol. Chem. Phys.* **1978**, *74*, 918–932.
80. Spina, R.; Spekowius, M.; Hopmann, C. Multiphysics simulation of thermoplastic polymer crystallization. *Mater. Des.* **2016**, *95*, 455–469.
81. Zheng, R.; Tanner, R.; Wo, D.L.; et al. Modeling of flow-induced crystallization of colored polypropylene in injection molding. *Korea-Aust. Rheol. J.* **2010**, *22*, 151–162.
82. Derakhshandeh, M.; Hatzikiriakos, S.G. Flow-induced crystallization of high-density polyethylene: the effects of shear and uniaxial extension. *Rheol. Acta* **2012**, *51*, 315–327.
83. Jalali, A.; Huneault, M.A.; Elkoun, S. Effect of thermal history on nucleation and crystallization of poly (lactic acid). *J. Mater. Sci.* **2016**, *51*, 7768–7779.
84. Jalali, A.; Shahbikian, S.; Huneault, M.A.; et al. Effect of molecular weight on the shear-induced crystallization of poly (lactic acid). *Polymer* **2017**, *112*, 393–401.
85. Jalali, A.; Huneault, M.A.; Elkoun, S. Effect of molecular weight on the nucleation efficiency of poly (lactic acid) crystalline phases. *J. Polym. Res.* **2017**, *24*, 182.
86. Jalali, A.; Huneault, M.A.; Nofar, M.; et al. Effect of branching on flow-induced crystallization of poly (lactic acid). *Eur. Polym. J.* **2019**, *119*, 410–420.
87. Housmans, J.W.; Peters, G.; Meijer, H. Flow-induced crystallization of propylene/ethylene random copolymers. *J. Therm. Anal. Calorim.* **2009**, *98*, 693–705.
88. Nafar Sefiddashti, M.H.; Edwards, B.J.; Khomami, B. Atomistic simulation of flow-induced microphase separation and crystallization of an entangled polyethylene melt undergoing uniaxial elongational flow and the role of Kuhn segment extension. *Polymers* **2023**, *15*, 1831.
89. Nafar Sefiddashti, M.H.; Edwards, B.J.; Khomami, B. Flow-induced phase phenomena in an entangled polyethylene/benzene solution under uniaxial elongational flow. *Rheol. Acta* **2024**, *63*, 113–133.
90. Nazari, B.; Rhoades, A.M.; Schaake, R.P.; et al. Flow-induced crystallization of PEEK: Isothermal crystallization kinetics and lifetime of flow-induced precursors during isothermal annealing. *Acs Macro Lett.* **2016**, *5*, 849–853.
91. Seo, J.; Parisi, D.; Gohn, A.M.; et al. Flow-induced crystallization of poly (ether ether ketone): Universal aspects of specific work revealed by corroborative rheology and x-ray scattering studies. *Macromolecules* **2020**, *53*, 10040–10050.
92. Zhang, Z.; Hatzikiriakos, S.G. Flow-induced crystallization of polylactides. *J. Rheol.* **2022**, *66*, 257–273.
93. Fernandez-Ballester, L.; Thurman, D.W.; Zhou, W.; et al. Effect of long chains on the threshold stresses for flow-induced

crystallization in iPP: Shish kebabs vs sausages. *Macromolecules* **2012**, *45*, 6557–6570.
94. Yaghini, N.; Peters, G.W. Modeling crystallization kinetics and resulting properties of polyamide 6. *Macromolecules* **2021**, *54*, 1894–1904.
95. Brucato, V.; Crippa, G.; Piccarolo, S.; et al. Crystallization of polymer melts under fast cooling. I: Nucleated polyamide 6. *Polym. Eng. Sci.* **1991**, *31*, 1411–1416.
96. Ziabicki, A. Theoretical Aspects of High-Speed Spinning. *Sen'I Gakkaishi* **1982**, *38*, P409–P417.
97. Caldas, V.; Brown, G.; Nohr, R.; et al. Enhancement of tensile properties of isotactic polypropylene spunbonded fabrics by a surface-modified silica/silicone copolymer additive. *J. Appl. Polym. Sci.* **1997**, *65*, 1759–1772.
98. Fakirov, S.; Kamo, H.; Evstatiev, M.; et al. Microfibrillar reinforced composites from PET/LDPE blends: Morphology and mechanical properties. *J. Macromol. Sci.-Phys.* **2004**, *43 B*, 775–789.
99. Vogel, R.; Gedan-Smolka, M.; Häussler, L.; et al. Evaluation of the crystallization of polypropylene at melt spinning conditions using the green chemical orotic acid as nucleating agent. *Adv. Res. Text. Eng.* **2018**, *3*, 1023.
100. Stolin, A.; Merzhanov, A.; Malkin, A.Y. Non-isothermal phenomena in polymer engineering and science: A review. Part I: Non-isothermal polymerization. *Polym. Eng. Sci.* **1979**, *19*, 1065–1073.
101. Stolin, A.; Merzhanov, A.; Malkin, A.Y. Non-isothermal phenomena in polymer engineering and science: A review. Part II: Non-isothermal phenomena in polymer deformation. *Polym. Eng. Sci.* **1979**, *19*, 1074–1080.
102. Thomas, S.; Grohens, Y.; Jyotishkumar, P. *Characterization of Polymer Blends: Miscibility, Morphology and Interfaces*; John Wiley & Sons: Hoboken, NJ, USA, 2015.
103. Ziabicki, A. Mechanical aspects of fibre spinning process in molten polymers—Part III: Tensile force and stress. *Kolloid-Z.* **1961**, *175*, 14–27.
104. Pantani, R.; Coccorullo, I.; Speranza, V.; et al. Modeling of morphology evolution in the injection molding process of thermoplastic polymers. *Prog. Polym. Sci.* **2005**, *30*, 1185–1222.
105. Pantani, R.; Speranza, V.; Titomanlio, G. Simultaneous morphological and rheological measurements on polypropylene: Effect of crystallinity on viscoelastic parameters. *J. Rheol.* **2015**, *59*, 377–390.
106. Zhao, B. Numerical simulation and experimental study of the polypropylene polymer air drawing model and air jet flow field model in the spunbonding nonwoven process. *Ind. Eng. Chem. Res.* **2013**, *52*, 11061–11069.
107. Kanai, T.; Kohri, Y.; Takebe, T. Theoretical analysis of the spunbond process and its applications for polypropylenes. *Adv. Polym. Technol.* **2018**, *37*, 2085–2094.
108. Sbirrazzuoli, N. Determination of pre-exponential factors and of the mathematical functions $f(\alpha)$ or $G(\alpha)$ that describe the reaction mechanism in a model-free way. *Thermochim. Acta* **2013**, *564*, 59–69.
109. Chen, T.; Zhang, C.; Li, L.; et al. Simulating the drawing of spunbonding nonwoven process using an artificial neural network technique. *J. Text. Inst.* **2008**, *99*, 479–488.
110. Kase, S.; Matsuo, T. Studies on melt spinning. I. Fundamental equations on the dynamics of melt spinning. *J. Polym. Sci. Part Gen. Pap.* **1965**, *3*, 2541–2554.
111. Nie, C.; Peng, F.; Xu, T.Y.; et al. A unified thermodynamic model of flow-induced crystallization of polymer. *Chin. J. Polym. Sci.* **2021**, *39*, 1489–1495.
112. Sheng, J.; Chen, W.; Cui, K.; et al. Polymer crystallization under external flow. *Rep. Prog. Phys.* **2022**, *85*, 036601.
113. Tabatabaei, A.; Park, C.B. In-situ visualization of PLA crystallization and crystal effects on foaming in extrusion. *Eur. Polym. J.* **2017**, *96*, 505–519.
114. Tabatabaei, A.; Barzegari, M.R.; Mark, L.H.; et al. Visualization of polypropylene's strain-induced crystallization under the influence of supercritical CO2 in extrusion. *Polymer* **2017**, *122*, 312–322.
115. Flory, P.J. Thermodynamics of crystallization in high polymers. I. Crystallization induced by stretching. *J. Chem. Phys.* **1947**, *15*, 397–408.
116. Haas, T.W.; Maxwell, B. Effects of shear stress on the crystallization of linear polyethylene and polybutene-1. *Polym. Eng. Sci.* **1969**, *9*, 225–241.
117. Guo, J.; Narh, K.A. Simplified model of stress-induced crystallization kinetics of polymers. *Adv. Polym. Technol. J. Polym. Process. Inst.* **2002**, *21*, 214–222.
118. Kim, K.H.; Isayev, A.; Kwon, K. Flow-induced crystallization in the injection molding of polymers: A thermodynamic approach. *J. Appl. Polym. Sci.* **2005**, *95*, 502–523.
119. Ziabicki, A.; Jarecki, L. Crystallization-controlled limitations of melt spinning. *J. Appl. Polym. Sci.* **2007**, *105*, 215–223.
120. Tanner, R.I.; Qi, F. Stretching, shearing and solidification. *Chem. Eng. Sci.* **2009**, *64*, 4576–4579.
121. Rong, Y.; He, H.; Cao, W.; et al. Multi-scale molding and numerical simulation of the flow-induced crystallization of polymer. *Comput. Mater. Sci.* **2013**, *67*, 35–39.
122. Zheng, R.; Kennedy, P. A model for post-flow induced crystallization: General equations and predictions. *J. Rheol.* **2004**, *48*, 823–842.
123. Graessley, W.W. Some phenomenological consequences of the Doi–Edwards theory of viscoelasticity. *J. Polym. Sci. Polym. Phys. Ed.* **1980**, *18*, 27–34.
124. Acierno, S.; Coppola, S.; Grizzuti, N.; et al. Coupling between kinetics and rheological parameters in the flow-induced

crystallization of thermoplastic polymers. *Macromol. Symp.* **2002**, *185*, 233–241.
125. Nozaki, D.; Mai, T.T.; Tsunoda, K.; et al. Tracking the Evolution of Heterogeneous Crystallization Driven by Complex Deformation Scenarios in Natural Rubber. *Macromolecules* **2025**, *58*, 4059–4069.
126. ANSYS, Inc. ANSYS Polyflow, Release 2023 R1. 2023. Available online: https://www.ansys.com/products/fluids/ansys-polyflow (accessed on 1 September 2024).
127. Azahar, A.A.B. Numerical Simulation for Polymer Blend using OpenFOAM. Ph.D. Thesis, The University of Leeds, Leeds, UK, 2020.
128. Ataei, M.; Shaayegan, V.; Costa, F.; et al. LBfoam: An open-source software package for the simulation of foaming using the Lattice Boltzmann Method. *Comput. Phys. Commun.* **2021**, *259*, 107698.
129. Ataei, M.; Bussmann, M.; Shaayegan, V.; et al. NPLIC: A machine learning approach to piecewise linear interface construction. *Comput. Fluids* **2021**, *223*, 104950.
130. Hadinata, C.; Boos, D.; Gabriel, C.; et al. Elongation-induced crystallization of a high molecular weight isotactic polybutene-1 melt compared to shear-induced crystallization. *J. Rheol.* **2007**, *51*, 195–215.
131. Comminal, R.; Pimenta, F.; Hattel, J.H.; et al. Numerical simulation of the planar extrudate swell of pseudoplastic and viscoelastic fluids with the streamfunction and the VOF methods. *J. Non-Newton. Fluid Mech.* **2018**, *252*, 1–18.
132. Doufas, A.K.; Dairanieh, I.S.; McHugh, A.J. A continuum model for flow-induced crystallization of polymer melts. *J. Rheol.* **1999**, *43*, 85–109.
133. Doufas, A.K.; McHugh, A.J.; Miller, C. Simulation of melt spinning including flow-induced crystallization Part I. Model development and predictions. *J. -Non-Newton. Fluid Mech.* **2000**, *92*, 27–66.
134. Kühn, K. Segment-long-spacing crystallites, a powerful tool in collagen research. *Collagen Relat. Res.* **1982**, *2*, 61–81.
135. Doufas, A.K.; McHugh, A.J. Simulation of film blowing including flow-induced crystallization. *J. Rheol.* **2001**, *45*, 1085–1104.
136. Kohler, W.; Shrikhande, P.; McHugh, A. Modeling melt spinning of PLA fibers. *J. Macromol. Sci. Part Phys.* **2005**, *44*, 185–202.
137. Kohler, W.H.; McHugh, A.J. 2D Modeling of high-speed fiber spinning with flow-enhanced crystallization. *J. Rheol.* **2007**, *51*, 721–733.
138. Patel, R.M.; Doufas, A.K.; Paradkar, R.P. Raman spectroscopy for spinline crystallinity measurements. II. Validation of fundamental fiber-spinning models. *J. Appl. Polym. Sci.* **2008**, *109*, 3398–3412.
139. Dhadwal, R. Numerical simulation of a two-phase melt spinning model. *Appl. Math. Model.* **2011**, *35*, 2959–2971.
140. Spina, R.; Spekowius, M.; Hopmann, C. Multiscale Modeling of Polymer Crystallization. In Proceedings of the 2013 COMSOL Conference, Rotterdam, The Netherlands, 23–25 October 2013.
141. Spina, R.; Spekowius, M.; Hopmann, C. Multi-scale thermal simulation of polymer crystallization. *Int. J. Mater. Form.* **2015**, *8*, 497–504.
142. Spekowius, M.; Spina, R.; Hopmann, C. Mesoscale simulation of the solidification process in injection moulded parts. *J. Polym. Eng.* **2016**, *36*, 563–573.
143. Roozemond, P.C.; Steenbakkers, R.J.; Peters, G.W. A Model for Flow-enhanced Nucleation Based on Fibrillar Dormant Precursors. *Macromol. Theory Simulations* **2011**, *20*, 93–109.
144. Roozemond, P.C.; van Drongelen, M.; Ma, Z.; et al. Self-Regulation in Flow-Induced Structure Formation of Polypropylene. *Macromol. Rapid Commun.* **2015**, *36*, 385–390.
145. Roozemond, P.C.; Ma, Z.; Cui, K.; et al. Multimorphological crystallization of shish-kebab structures in isotactic polypropylene: Quantitative modeling of parent–daughter crystallization kinetics. *Macromolecules* **2014**, *47*, 5152–5162.
146. Ghosal, A.; Sinha-Ray, S.; Yarin, A.L.; et al. Numerical prediction of the effect of uptake velocity on three-dimensional structure, porosity and permeability of meltblown nonwoven laydown. *Polymer* **2016**, *85*, 19–27.
147. Ghosal, A.; Chen, K.; Sinha-Ray, S.; et al. Modeling polymer crystallization kinetics in the meltblowing process. *Ind. Eng. Chem. Res.* **2019**, *59*, 399–412.
148. Chen, K.; Ghosal, A.; Yarin, A.L.; et al. Modeling of spunbond formation process of polymer nonwovens. *Polymer* **2020**, *187*, 121902.
149. Yarin, A.; Sinha-Ray, S.; Pourdeyhimi, B. Meltblowing: Multiple polymer jets and fiber-size distribution and lay-down patterns. *Polymer* **2011**, *52*, 2929–2938.
150. Venu, L.B.S.; Shim, E.; Anantharamaiah, N.; et al. Three-dimensional structural characterization of nonwoven fabrics. *Microsc. Microanal.* **2012**, *18*, 1368–1379.
151. Rahman, S.M.; Rahman, S.; Tafreshi, H.V.; et al. CFD-DEM simulation of air-assisted electrospinning. *Chem. Eng. J.* **2025**, *503*, 158370.
152. Balakrishnan, V.K.; Pourdeyhimi, B.; Yarin, A.L. Numerical investigation of roping in multi-die meltblowing. *J. Appl. Phys.* **2024**, *135*.
153. Santoro, L.A.; Fischer, M.; Spoerer, Y.; et al. Experimental Determination of the Nakamura Crystallization Model Parameters of Isotactic Polypropylene (iPP). *SSRN* **2024**, SSRN 4791987. http://dx.doi.org/10.2139/ssrn.4791987.
154. Saad, S.; Cruz, C.; Régnier, G.; et al. Efficient identification of a flow-induced crystallization model for injection molding simulation. *Int. J. Adv. Manuf. Technol.* **2024**, *133*, 5243–5270.

155. Grosso, G.; Troisi, E.M.; Jaensson, N.O.; et al. Modelling flow induced crystallization of IPP: Multiple crystal phases and morphologies. *Polymer* **2019**, *182*, 121806.
156. van Berlo, F.P.; Cardinaels, R.; Peters, G.W.; et al. A numerical study of extensional flow-induced crystallization in filament stretching rheometry. *Polym. Cryst.* **2021**, *4*, e10154.
157. Roozemond, P.C.; van Drongelen, M.; Ma, Z.; et al. Modeling flow-induced crystallization in isotactic polypropylene at high shear rates. *J. Rheol.* **2015**, *59*, 613–642.
158. Lavine, M.S.; Waheed, N.; Rutledge, G.C. Molecular dynamics simulation of orientation and crystallization of polyethylene during uniaxial extension. *Polymer* **2003**, *44*, 1771–1779.
159. Dukovski, I.; Muthukumar, M. Langevin dynamics simulations of early stage shish-kebab crystallization of polymers in extensional flow. *J. Chem. Phys.* **2003**, *118*, 6648–6655.
160. Mohajer, B.; Kheradmandkeysomi, M.; Amirzadeh, S.; et al. Simplified Dual-Scale Simulation Framework for Computational Modeling of Nanofibrillation Phenomena Via Fiber in Fiber Technology with Experimental Data. *Eng. Comput.* **2026**, *in press*.
161. Mohajer, B.; Kheradmandkeysomi, M.; Park, C.B.; et al. Enhancing Drafter Performance in Spunbonding of Polymeric Fibers via Airflow Simulation. *Polymers* **2026**, *18*, 187.
162. Mead, D.W.; Leal, L.G. The reptation model with segmental stretch: I. Basic equations and general properties. *Rheol. Acta* **1995**, *34*, 339–359.
163. Plimpton, S. Fast parallel algorithms for short-range molecular dynamics. *J. Comput. Phys.* **1995**, *117*, 1–19.
164. Read, D.J.; McIlroy, C.; Das, C.; et al. PolySTRAND model of flow-induced nucleation in polymers. *Phys. Rev. Lett.* **2020**, *124*, 147802.
165. Graham, R.S.; Olmsted, P.D. Coarse-grained simulations of flow-induced nucleation in semicrystalline polymers. *Phys. Rev. Lett.* **2009**, *103*, 115702.
166. Nicholson, D.A.; Rutledge, G.C. Molecular simulation of flow-enhanced nucleation in n-eicosane melts under steady shear and uniaxial extension. *J. Chem. Phys.* **2016**, *145*, 244903 .
167. Nicholson, D.A.; Rutledge, G.C. An assessment of models for flow-enhanced nucleation in an n-alkane melt by molecular simulation. *J. Rheol.* **2019**, *63*, 465–475.
168. Koyama, A.; Yamamoto, T.; Fukao, K.; et al. Molecular dynamics simulation of polymer crystallization from an oriented amorphous state. *Phys. Rev. E* **2002**, *65*, 050801.
169. Luo, C.; Kröger, M.; Sommer, J.U. Molecular dynamics simulations of polymer crystallization under confinement: Entanglement effect. *Polymer* **2017**, *109*, 71–84.
170. Sigalas, N.I.; Van Kraaij, S.A.; Lyulin, A.V. Effect of Temperature on Flow-Induced Crystallization of Isotactic Polypropylene: A Molecular-Dynamics Study. *Macromolecules* **2023**, *56*, 8417–8427.
171. Kheradmandkeysomi, M.; Salehi, A.; Jalali, A.; et al. Achieving super-tough high-density polyethylene with promising foamability using silane crosslinked polyolefin elastomer nanofibrils network. *Compos. Sci. Technol.* **2024**, *251*, 110576.
172. Kheradmandkeysomi, M.; Salehi, A.; Jalali, A.; et al. Enhancing Mechanical Performance of High-Density Polyethylene at Different Environmental Conditions with Outstanding Foamability through In-Situ Rubber Nanofibrillation: Exploring the Impact of Interface Modification. *Acs Appl. Mater. Interfaces* **2024**, *16*, 29291–29304.
173. Mohajer, B. rheoFibrillator: OpenFOAM-Based Simulation Tool for Rheology and Fibrillation, Version 1.0.0. Available online: https://github.com/behrang-mohajer/rheoFibrillator (accessed on 1 December 2025)
174. Zhao, B. Modeling polypropylene polymer air drawing in the spunbonding nonwoven process. *Int. J. Cloth. Sci. Technol.* **2014**, *26*, 184–194.
175. Bo, Z. Experimental and Numerical Simulation Study of an Air drawing Model of Polyethylene Terephthalate (PET) Polymer and Model of Air Jet Flow Field in the Spunbonding Nonwoven Process. *Fibres Text. East. Eur.* **2014**, pp. 89–96.
176. Papanastasiou, A.; Scriven, L.; Macosko, C. An integral constitutive equation for mixed flows: viscoelastic characterization. *J. Rheol.* **1983**, *27*, 387–410.
177. Grice, A. Modelling the creation of polymer fibres for nonwoven fabrics. Ph.D. Thesis, Loughborough University, Loughborough, UK, 2018.
178. Liu, J.; Anderson, K.L.; Sridhar, N. Direct Simulation of Polymer Fused Deposition Modeling (FDM)-An Implementation of the Multi-Phase Viscoelastic Solver in OpenFOAM. *Int. J. Comput. Methods* **2020**, *17*, 1844002.
179. Voller, V.R.; Prakash, C. A fixed grid numerical modelling methodology for convection-diffusion mushy region phase-change problems. *Int. J. Heat Mass Transf.* **1987**, *30*, 1709–1719.
180. Höhnemann, T.; Schnebele, J.; Arne, W.; et al. Nanoval Technology—An Intermediate Process between Meltblown and Spunbond. *Materials* **2023**, *16*, 2932.
181. Wienke, S.; Spekowius, M.; Dammer, A.; et al. Towards an accurate simulation of the crystallisation process in injection moulded plastic components by hybrid parallelisation. *Int. J. High Perform. Comput. Appl.* **2014**, *28*, 356–367.
182. Speranza, V.; Liparoti, S.; Volpe, V.; et al. Modelling of morphology development towards spherulites and shish–kebabs: Application to isothermal flow-induced crystallization experiments on isotactic polypropylene. *Polymer* **2020**, *196*, 122459.
183. Speranza, V.; Liparoti, S.; Titomanlio, G.; et al. Modeling spherulitic and fibrillar crystallization kinetics in injection

molding: Analysis of process variables and morphological evolution. *Polymer* **2024**, *312*, 127647.
184. Andreev, M.; Nicholson, D.A.; Kotula, A.; et al. Rheology of crystallizing LLDPE. *J. Rheol.* **2020**, *64*, 1379–1389.
185. Battocchio, F.; Sutcliffe, M.; Teschner, F. Fibre behaviour in the spunbonding process. Part II: Modelling fibre dynamics in the diffuser. *Proc. Inst. Mech. Eng. Part J. Mech. Eng. Sci.* **2017**, *231*, 407–417.
186. Boudaghi, M.; Edwards, B.J.; Khomami, B. Molecular Processes Leading to Shear Banding in Entangled Polymeric Solutions. *Polymers* **2023**, *15*, 3264.
187. Nafar Sefiddashti, M.H.; Edwards, B.J.; Khomami, B. A thermodynamically inspired method for quantifying phase transitions in polymeric liquids with application to flow-induced crystallization of a polyethylene melt. *Macromolecules* **2020**, *53*, 10487–10502.
188. Gangal, C.S.; Rutledge, G.C. Molecular simulation of flow-enhanced nucleation of polyethylene crystallites in biaxial flows. *J. Chem. Phys.* **2024**, *160*.
189. Hussain, M.A.; Aoyagi, T.; Kikutani, T.; et al. Lamellar Orientation Analysis and Mechanical Properties of Polyethylene in Stretch-Induced Crystallization. *Polymers* **2025**, *17*, 1450.
190. Amirabadi, S.; Kheradmandkeysomi, M.; Zandieh, A.; et al. Highly tough and flame retardant polystyrene composites by elastomeric nanofibers and hexagonal boron nitride. *J. Mater. Sci. Technol.* **2024**, *198*, 208–220.
191. Chang, B.; Schneider, K.; Vogel, R.; et al. Influence of nucleating agent self-assembly on structural evolution of isotactic polypropylene during uniaxial stretching. *Polymer* **2018**, *138*, 329–342.
192. Jayanarayanan, K.; Jose, T.; Thomas, S.; et al. Effect of draw ratio on the microstructure, thermal, tensile and dynamic rheological properties of insitu microfibrillar composites. *Eur. Polym. J.* **2009**, *45*, 1738–1747.
193. Wang, H.; Jin, X.; Mao, N.; et al. Differences in the Tensile Properties and Failure Mechanism of PP/PE Core/Sheath Bicomponent and PP Spunbond Fabrics in Uniaxial Conditions. *Text. Res. J.* **2010**, *80*, 1759–1767.
194. Arvidson, S.A.; Wong, K.C.; Gorga, R.E.; et al. Structure, molecular orientation, and resultant mechanical properties in core/sheath poly (lactic acid)/polypropylene composites. *Polymer* **2012**, *53*, 791–800.
195. Anstey, A.; Tuccitto, A.V.; Lee, P.C.; et al. Generation of tough, stiff polylactide nanocomposites through the in situ nanofibrillation of thermoplastic elastomer. *Acs Appl. Mater. Interfaces* **2022**, *14*, 14422–14434.
196. Jalali, A.; Romero-Diez, S.; Nofar, M.;et al. Entirely environment-friendly polylactide composites with outstanding heat resistance and superior mechanical performance fabricated by spunbond technology: Exploring the role of nanofibrillated stereocomplex polylactide crystals. *Int. J. Biol. Macromol.* **2021**, *193*, 2210–2220.